Atmospheric Research 272 (2022) 106155

Contents lists available at ScienceDirect

Atmospheric Research

journal homepage: www.elsevier.com/locate/atmosres

Effect of data assimilation in the Polar WRF with 3DVAR on the prediction of radiation, heat flux, cloud, and near surface atmospheric variables over Svalbard

Dae-Hui Kim, Hyun Mee Kim *

Atmospheric Predictability and Data Assimilation Laboratory, Department of Atmospheric Sciences, Yonsei University, Seoul, Republic of Korea

ARTICLE INFO

Keywords:
Polar Weather Research and forecasting (WRF) model
Three-dimensional variational (3DVAR) data assimilation
Prediction of radiation, heat flux, cloud, and near surface atmospheric variables over Svalbard
Satellite data assimilation
Uncertainty of the Arctic forecast

ABSTRACT

Although the Polar Weather Research and Forecasting (PWRF) model has been developed for polar environments, simulations of atmospheric states in the polar region still have large uncertainties. Therefore, the effects of data assimilation (DA) to improve forecasts in the polar region were investigated for September 2017 using PWRF and the three-dimensional variational (3DVAR) DA method. The experiments without DA and those with DA assimilating only conventional observations and both conventional observations and satellite radiance data were performed. The forecasts from all experiments both without and with DA underestimated (overestimated) the downward longwave (shortwave) radiation flux due to the underestimation of the amount of Arctic clouds. When satellite radiance data (i.e., the Advanced Microwave Sounding Unit-A (AMSU-A) and Microwave Humidity Sounder (MHS)) were assimilated in addition to conventional observations in the PWRF, the distribution and amount of water vapor became closer to observations, which improves cloud liquid water forecasts. Therefore, when both conventional observations and radiance data were assimilated, the 25–30 h forecast errors of the downward longwave and shortwave radiation fluxes and sensible and latent heat fluxes decreased by 12.7%, 8.1%, 3.2%, and 7.8% with the WSM5 scheme and by 17.1%, 4.7%, 2.5%, and 3.1% with the 2-moment Morrison scheme, respectively, compared to those in the experiments without DA. The forecast errors of the 10 m wind and 2 m temperature with DA were smaller than those without DA at most observation stations. Therefore, the uncertainties of the Arctic forecasts in the PWRF decreased when using DA. To further improve Arctic forecasts, the assimilation of various additional satellite data is necessary.

1. Introduction

Compared to the Antarctic, the effects of abrupt climate change are more noticeable in the Arctic, and the climate change in the Arctic affects extreme weather events in mid-latitudes (Francis and Vavrus, 2012; Cohen et al., 2014). The Arctic climate change is characterized by amplified warming in the Arctic compared to mid-latitudes (Overland et al., 2016). The Arctic warming causes changes in the surface energy budget (Semmler et al., 2012), deepening of the Arctic boundary layers, and increased cloudiness (Francis et al., 2009) over the Arctic. In addition, the Arctic warming weakens the polar jet due to a decrease in the poleward atmospheric thickness gradients (Overland and Wang, 2010) and causes variations in Asian monsoon patterns (Zhao et al., 2004). Therefore, it is important to accurately predict the weather and climate of the Arctic based on our knowledge of specific Arctic environments.

To understand the interactions between many factors affecting atmospheric conditions in the Arctic, several observation campaigns have been performed. During 1997–98, the Surface Heat Budget of the Arctic Ocean (SHEBA) experiment was conducted to analyze the interactions between the ocean, ice, and atmosphere (Uttal et al., 2002). To verify the characteristics of Arctic clouds and their influence on the atmosphere, the Arctic Summer Cloud-Ocean Study (ASCOS) (August–September 2008) was conducted during the International Polar Year period, and it was found that the low concentration of cloud condensation nuclei in the Arctic contributes to formation and maintenance of optically thin low-level cloud in the Arctic (Tjernström et al., 2014). Based on the findings in the ASCOS, the cloud microphysics scheme in the Polar Weather Research and Forecasting (PWRF) model was optimized for the Arctic environment (Hines and Bromwich, 2017). The Arctic Clouds in

* Corresponding author at: Department of Atmospheric Sciences, Yonsei University, 50 Yonsei-ro, Seodaemun-gu, Seoul 03722, Republic of Korea.
E-mail address: khm@yonsei.ac.kr (H.M. Kim).

https://doi.org/10.1016/j.atmosres.2022.106155
Received 20 April 2021; Received in revised form 2 March 2022; Accepted 21 March 2022
Available online 23 March 2022

Summer Experiment (ACSE) was conducted from July to October 2014, and investigated the interaction of surface conditions, boundary layer structure, and cloud properties for the transition period from sea ice melting to sea ice freezing. Based on the measurements in the ACSE, Sotiropoulou et al. (2016) found that the atmospheric processes associated with the sea ice melting and freezing near the ice edge can be different from those on the central ice pack. From 2015 to 2017, the Atmospheric Radiation Measurement (ARM) West Antarctic Radiation Experiment (AWARE) was performed to investigate the surface energy budgets and cloud properties in the Antarctic, and it was found that cloud microphysical properties in the Antarctic are different from those in the Arctic (Lubin et al., 2020). Based on AWARE data, the cloud microphysics scheme in the PWRF model was optimized for the Antarctic environment (Hines et al., 2021). In addition, modeling studies have been performed to enhance the forecast accuracy based on the knowledge gained from observation campaigns (Wyser et al., 2008; Loewe et al., 2017).

Recently, the PWRF model has been optimally developed specifically for Arctic environments (Hines and Bromwich, 2008). Detailed sea ice information was considered in the PWRF (Bromwich et al., 2009; Hines et al., 2015), and the performance of the model has been verified for various cases (Hines et al., 2011; Wilson et al., 2011; Seo and Yang, 2013; Bromwich et al., 2016; Kim et al., 2019). Despite these efforts, the simulations for the surface energy balance still have large uncertainties due to uncertainties in cloud simulations in the Arctic region. Wesslén et al. (2014) compared two different forecasts in the PWRF, one using a WRF single-moment 5-class cloud microphysics scheme (WSM5) (Hong et al., 2004) and the other using a 2-moment Morrison cloud microphysics scheme (Morrison et al., 2005), and verified the results against observations in ASCOS data. The results showed that both forecasts had limitations in cloud simulations, but the 2-moment Morrison scheme performed better than the WSM5 scheme, which suggests that reflecting the effect of interactions between aerosol and cloud is essential for the modeling. Furthermore, to simulate Arctic low-level clouds accurately, Hines and Bromwich (2017) improved the forecast accuracy of the radiation by optimizing the liquid cloud droplet concentration in the 2-moment Morrison scheme to the Arctic environment, based on observed cloud nuclei concentration data. Currently, the PWRF, optimized to the polar region through several previous studies, is used for the operational Antarctic Mesoscale Prediction System (AMPS) and Arctic System Reanalysis (ASR) v2. Hines et al. (2019) compared the performances of the WSM5, 2-moment Morrison, and two newly added schemes in the WRF model (i.e., Thompson aerosol-aware scheme (Thompson and Eidhammer, 2014) and P3 scheme (Morrison and Milbrandt, 2015)), and showed that 2-moment Morrison, Thompson aerosol-aware, and P3 schemes still had uncertainties in cloud simulations, but their errors were smaller than those of WSM5. In contrast, they also found that the forecast accuracy of near-surface variables was similar between experiments using different microphysics schemes or most accurate when the WSM5 was used (Hines et al., 2019), which implies that the performance of the microphysics scheme varies depending on the variables simulated.

Unlike studies that have attempted to simulate the polar atmosphere (e.g., radiation, heat flux, and cloud) more accurately by improving the microphysics scheme, studies on improving polar atmosphere (e.g., radiation, heat flux, and cloud) simulation using data assimilation (DA) have rarely been performed. The improvement of the microphysics scheme reduces the model error in cloud simulations, whereas DA reduces the initial condition error of the forecast. Reducing both the model error and initial condition error is expected to be beneficial for enhancing the forecast accuracy of Arctic clouds as well as other atmospheric variables in the Arctic. The model performance with the improved microphysics scheme can be further enhanced when the initial condition of the model is improved using DA. Due to projects such as the Year of Polar Prediction (2017–19) and the resulting high-quality polar observations, the DA effect on the predictability improvement over the polar region is expected to be positive. Despite this effort, previous studies on the effects of DA on forecast improvement in the polar region have been restricted to observation data from specific campaigns and mainly focused on in situ type observations (i.e., sonde or buoy) rather than satellite data. In situ observations are more coarsely distributed in the Arctic than in midlatitudes (Jung et al., 2016). Unlike in situ observations, satellite observations can monitor the entire Arctic region, and assimilation of satellite observations improves vertical temperature and humidity simulations in the Arctic (Randriamampianina et al., 2019). The use and impact of satellite data in polar regions need to be enhanced (Jung et al., 2016). Therefore, to improve the forecast accuracy of Arctic weather using PWRF, the DA of various observations, including satellite radiance data, is necessary.

In this study, the effect of assimilating conventional observations and satellite radiance data around Svalbard, Norway on forecasts was evaluated using the high-resolution PWRF model with the three-dimensional variational (3DVAR) DA system. In cases where the existing microphysics scheme of the PWRF could not accurately simulate Arctic atmospheric states (i.e., radiation, heat flux, cloud properties, and near surface atmospheric variables, etc.), the effect of DA on reducing the errors in both the initial conditions and forecasts was evaluated. In addition, forecast sensitivity to the microphysics scheme was also analyzed using the two schemes of WSM5 and 2-moment Morrison. Section 2 presents the detailed methodology and information regarding the observations used. Sections 3 and 4 consist of the results and a summary with discussion, respectively.

2. Methodology

2.1. Model and data assimilation

PWRF v3.7.1, which was developed to reflect the environmental characteristics in the polar region, was used in this study. Experimental domain 1 consisted of 15 km horizontal grid resolution with 721 × 721 grid points, which followed the setup of ASRv2 (Bromwich et al., 2018), and the vertical model levels were 51 with a model top at 10 hPa. Domains 2 and 3 were located in Svalbard. Domain 2 was configured to minimize the effect of sudden altitude variations on the east coast of Greenland in the western boundary (Fig. 1a). One-way nesting was applied to domains 1 and 2, and domains 2 and 3. The horizontal grid resolutions of domains 2 and 3 were 5 km (283 × 229) and 1.67 km (400 × 442), respectively. The vertical levels of domains 2 and 3 are the same as in domain 1. The European Center or Medium-range Weather Forecasts (ECMWF) ERA5 0.25° × 0.25° reanalysis data were used as the boundary conditions updated every 6 h of the cycling experiments and as the initial condition once at the beginning of the cycling experiments.

The physics schemes appropriate for PWRF (Bromwich et al., 2013) were used in this study. The parameterization schemes consist of the Rapid Radiative Transfer Model for Global Climate Models (Iacono et al., 2008) for short-and long-wave radiation, the optimized Noah land surface model (Chen et al., 1996) for land surface, the Monin–Obukhov (Monin and Obukhov, 1954) for surface layer, and the Mellor–Yamada–Janjic turbulent kinetic energy (Janjic, 1994) for planetary boundary layer. The Grell–Devenyi ensemble (Grell and Dévényi, 2002) for cumulus parameterization was used only for domain 1. For microphysics, the WSM5 and 2-moment Morrison scheme (hereafter Morrison) were used alternately. Hines et al. (2019) showed that the WSM5 scheme simulates temperature profiles relatively well but tends to simulate specific humidity less well than other schemes, which leads to the underestimation of the cloud amount in the model. Except for the cloud amount, the WSM5 simulates other variables comparable to or slightly better than other microphysics schemes, which makes the WSM5 used for AMPS. Morrison simulated the clouds better than WSM5, and the forecast accuracy of other variables with Morrison has also been verified (Hines et al., 2019). Therefore, in this study, the forecast accuracies when using WSM5 and Morrison were compared.

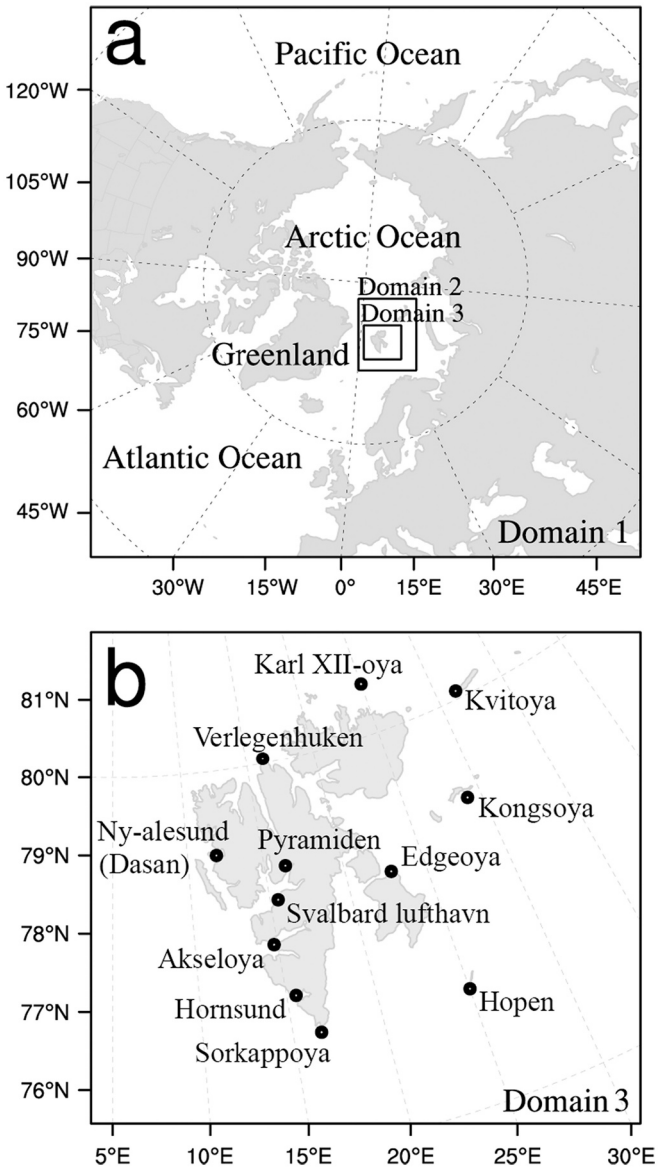

Fig. 1. (a) The domain for experiments. (b) The location of surface synoptic observations from land stations (SYNOP) in domain 3 used for verification.

The sea surface temperature was updated using ERA5 data at 6 h intervals, and the effect of the fractional sea ice was considered. During the experimental period, very little sea ice existed over the northwestern region of domain 2. Because sea ice affects the energy exchange between the lower atmosphere and the ocean, it is necessary to consider appropriate sea ice information in the PWRF. The PWRF is known for its ability to reflect detailed sea ice information (i.e., sea ice cover, sea ice thickness, sea ice albedo, and snow depth on sea ice) (Hines et al., 2015). Therefore, in this study, the sea ice cover of ERA5 was used and updated with 24 h intervals, and the sea ice thickness, sea ice albedo, and snow depth over sea ice were set by default values of 3 m, 0.65, and 1 m, respectively, in the PWRF.

Data assimilation was performed every 6 h in domain 2 using the WRFDA v3.8 3DVAR system. The conventional observations and microwave satellite radiance data (i.e., Advanced Microwave Sounding Unit-A (AMSU-A) and Microwave humidity Sounder (MHS)) were assimilated with ±3 h window at each analysis time (00, 06, 12, and 18 UTC). The Community Radiative Transfer Model (CRTM) was used, and the Variational Bias Correction (VarBC) was applied to assimilate radiance data. Because the field of view (FOV) is different for each satellite sensor, the AMSU-A and MHS data were thinned by 90 and 60 km, respectively. The background error covariance was calculated using the National Meteorological Center (NMC) method (Parrish and Derber, 1992) by using the differences between 12 h and 24 h forecasts during September 2017.

2.2. Observational data

The conventional observations and satellite radiance data, used in the National Centers for Environmental Prediction (NCEP) Global Data Assimilation System (GDAS), were assimilated in the PWRF 3DVAR system. Although the general in situ type observations (i.e., buoy, synop, metar, ships, and sonde) were consistently assimilated, the atmospheric motion vectors and sea winds produced from the satellites did not exist in domain 2 at certain times during the experimental period. The AMSU-A and MHS are sensitive to the vertical distributions of temperature and humidity, respectively. Therefore, the AMSU-A channels 5–9 and MHS channels 3–5, which are the same channels used for ASRv2, were assimilated. Because of the quality issues, the AMSU-A channels 7 and 8 in METOP-2, channel 9 in NOAA-18, channel 8 in NOAA-19, and MHS channel 3 in NOAA-19 were not assimilated (www.emc.ncep.noaa.gov/mmb/data_processing/Satellite_Historical_Documentation.htm).

Twelve World Meteorological Organization (WMO) surface synoptic observation (SYNOP) stations in Svalbard were used to evaluate the forecast accuracy of near-surface variables from the PWRF. Table 1 and Fig. 1b present detailed information on the locations of the WMO SYNOP stations. The highest 10 min average wind speed for the last 1 h, 2 m temperature, and sea level pressure observed every hour were used for verification. The downward longwave radiation flux (LWD) and downward shortwave radiation flux (SWD) observed every hour in Hopen (no. 11 in Table 1) were used for verification. In addition, the sensible heat flux (SHX) and latent heat flux (LHX) observed every hour at Dasan station (no. 13 in Table 1) located in Ny-ålesund were used for verification.

2.3. Experimental setting

The experimental period is from September 1 to 19, 2017, and this experimental period was selected because all observation variables for verification exist consistently for the period. The forecast accuracy of near-surface radiation, heat flux, and meteorological variables in the experiments with and without DA were evaluated for the period from September 6 to 19, 2017. Thus, the model spin-up period was set to 5 days from September 1 to 5, 2017.

Table 2 shows the configuration of all experiments. EXP1 was the experiment without DA, EXP2 was the experiment with DA that

Table 1
Locations of the surface synoptic observations from land stations (SYNOP) used for verification.

No.	Station name	Location		Classification
		Latitude [°N]	Longitude [°E]	
1	Sørkappøya	76.4777	16.5488	WMO site
2	Hornsund	77.0017	15.5358	
3	Verlegenhuken	80.0592	16.2500	
4	Akseløya	77.6888	14.7840	
5	Svalbard lufthavn	78.2453	15.5015	
6	Ny-ålesund	78.9243	11.9312	
7	Karl XII-oya	80.653	25.008	
8	Kvitoya	80.1017	31.462	
9	Kongsoya	78.7108	28.892	
10	Edgeoya-kapp heuglin	78.2508	22.8225	
11	Hopen	76.5097	25.0133	
12	Pyramiden	78.6557	16.3603	
13	Dasan (located in Ny-ålesund region)	78.9219	11.8658	Rep. of Korea site

Table 2
Details of all experiments.

Experiment	Microphysics scheme	Type	Observation
EXP1	WSM5	Experiment without DA	N/A
EXP2		Experiment with DA	Conventional obs.
EXP3			Conventional obs. + Microwave radiance (AMSU-A, MHS)
EXP4	Morrison 2-moment	Experiment without DA	N/A
EXP5		Experiment with DA	Conventional obs. + Microwave radiance (AMSU-A, MHS)

The conventional observation denotes all observation data in the prepBUFR files.

assimilated conventional observations, and EXP3 was the experiment with DA that assimilated conventional observations, AMSU-A, and MHA. EXP2 and 3 were performed to evaluate the effects of assimilating conventional and satellite observations in the cycling system. For EXP1, EXP2, and 3, WSM5 was used as the microphysics scheme. In EXP1, 48 h forecasts were produced at every analysis time (i.e., 00, 06, 12, and 18 UTC) using the ERA5 reanalysis as the initial and boundary conditions. In EXP2, the analyses were produced at every analysis time (i.e., 00, 06, 12, and 18 UTC) in domain 2 by assimilating conventional observations, and the 48 h forecasts were produced from those analyses. In EXP3, the radiance data of the AMSU-A and MHS were additionally assimilated to EXP2. EXP4 was the experiment without DA, using Morrison instead of WSM5. Except for using Morrison instead of WSM5, EXP5 had the same setup as EXP3. Thus, both EXP4 and 5 were performed to investigate the effect of Morrison instead of WSM5 on forecast performance.

To verify the forecasts of each experiment with the observations in Svalbard, the forecasts in domain 3 for each experiment were generated by the 1-way nesting of domain 2. The boundary conditions of domain 3 were obtained from the forecasts in domain 2. The first 24 h forecasts of each experiment were not used for verification by considering the time necessary to develop the planetary boundary layer reflecting the arctic surface characteristics and to adjust the hydrologic cycle (Hines and Bromwich, 2008; Kim et al., 2019). The bias and root-mean-square-error (RMSE) of each experiment were calculated for both 25–30 h and 25–48 h forecasts from 00, 06, 12, and 18 UTC (Table 3). For all experiments, the time series with 1 h intervals consisted of 25–30 h forecasts from 00, 06, 12, and 18 UTC, whereas 25–48 h forecasts from 00 UTC.

3. Results

3.1. Effect of data assimilation and microphysics on surface radiation

3.1.1. Bias and RMSE

Table 3 shows the average bias and RMSE for the LWD and SWD forecasts of each experiment against the observations in Hopen, Svalbard. The LWD showed a negative bias, whereas SWD showed a positive bias in all experiments. Due to the longer model spin-up time, the bias and RMSE of 25–48 h forecasts were smaller than those of the 25–30 h forecasts for all experiments. The forecasts in EXP2 with conventional observation DA were not distinctively accurate compared to those in EXP1 without DA. Regardless of the forecast time, the average bias and RMSE in EXP3 with DA of both conventional observations and satellite radiance data were smaller than those in EXP1 and 2, which indicates the importance of the satellite radiance DA. Compared to EXP1, the bias for the 25–30 h forecasts of LWD (SWD) in EXP3 was reduced by 32.3% (7.9%) and the RMSE for the 25–30 h forecasts of LWD (SWD) in EXP3 was reduced by 12.7% (8.1%). Compared to EXP2, the bias for the 25–30 h forecasts of LWD (SWD) in EXP3 was reduced by 29.3% (5.0%) and the RMSE for the 25–30 h forecasts of LWD (SWD) in EXP3 were reduced by 16.5% (5.6%). The RMSEs of LWD and SWD in EXP1 and 3 were further reduced in EXP4 and 5, respectively. The average bias and RMSE in EXP5 were smaller than those in EXP4. Compared to EXP1, the bias for the 25–30 h forecasts of LWD (SWD) in EXP5 was reduced by 28.7% (36.8%) and the RMSE for the 25–30 h forecasts of LWD (SWD) in EXP5 was reduced by 20.6% (29.3%). This implies that both LWD and SWD were simulated more accurately when using Morrison than WSM5.

3.1.2. Time series

Fig. 2 shows the time series of the 25–30 h forecasts for each experiment and observations for LWD and SWD. Diurnal variation did not clearly appear in the LWD (Fig. 2a), whereas this was clear in the SWD (Fig. 2b), similar to findings by Hines and Bromwich (2008). The SWD shows a diurnal variation due to the rotation of the Earth. In contrast, the LWD does not show a clear diurnal variation because the LWD is associated with the upward longwave radiative flux of the Earth which is always present regardless of the rotation of the Earth. Compared to observations, LWD (SWD) was generally underestimated (overestimated) in the model. This is because the model could not simulate well enough the thin clouds that were consistently present at low levels over the polar region (Wilson et al., 2012), although the amount of low-level clouds increased over the Arctic from August to September (Intrieri et al., 2002). These low-level clouds contributed to

Table 3
Average forecast error statistics for the longwave and shortwave downward radiation of each experiment and forecast time at the Hopen radiation observation station.

Variable	Experiment	25–30 h forecast		25–48 h forecast	
		Bias	RSME	Bias	RMSE
Longwave downward radiation ($W\ m^{-2}$)	EXP1	-8.152	21.138	-7.277	20.716
	EXP2	-7.807	22.092	-6.702	19.772
	EXP3	-5.518	18.445	-4.860	16.130
	EXP4	-8.414	20.250	-4.295	18.072
	EXP5	-5.814	16.787	-2.014	14.383
Shortwave downward Radiation ($W\ m^{-2}$)	EXP1	45.802	57.660	39.357	49.706
	EXP2	44.426	56.157	40.025	50.528
	EXP3	42.206	52.990	37.769	48.028
	EXP4	32.393	42.780	24.075	37.314
	EXP5	28.930	40.778	23.262	36.244

The grey shadings in EXP2, 3, 4, and 5 denotes the Bias and RMSE which were smaller (i.e., improved) compared to those in EXP1.

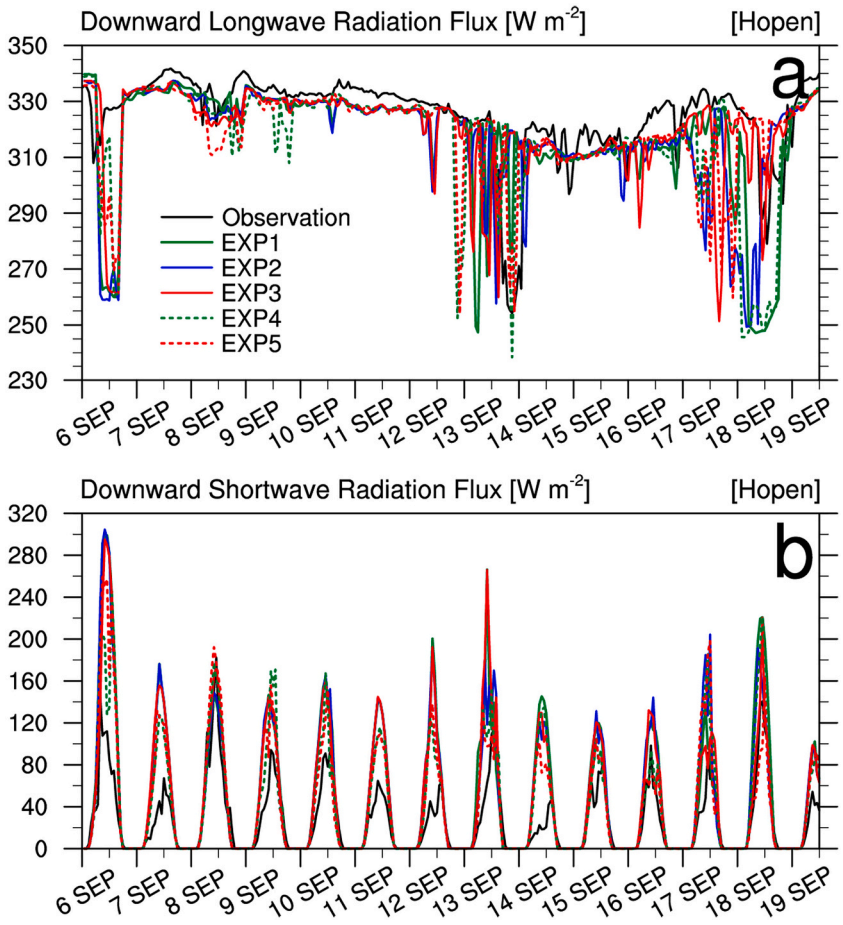

Fig. 2. Time series of observations and the 25–30 h forecasts of EXP1, EXP2, EXP3, EXP4, and EXP5 for (a) longwave downward radiation (W m^{-2}) and (b) shortwave downward radiation (W m^{-2}).

the increase of LWD and the decrease of SWD. The underestimation of the amount of low-level clouds has also been observed in ASRv2 and AMPS, which both used the PWRF (Bromwich et al., 2018; Hines et al., 2019). When the LWD and SWD observations varied suddenly, the variations of the LWD and SWD forecasts between the experiments were large. This is because simulating the episodic characteristic of radiation caused by variations in cloud information has large uncertainties, as shown in Bromwich et al. (2009).

The time-averaged observation value of the LWD was 324.9 W m^{-2} (Fig. 2a), which was similar to the average LWD values in both observations and forecasts during August in the SHEBA periods. The time averaged LWD values of 25–30 h (25–48 h) forecasts in EXP1, 2, 3, 4, and 5 were 316.7, 317.1, 319.4, 316.5 and 319.1 (317.6, 318.2, 320.0, 320.6 and 322.9) W m^{-2}, respectively. For the 25–30 h forecasts, the underestimation of LWD in the model was improved the most in EXP3. The underestimation of the modeled LWD improved the most in the 25–48 h forecasts of EXP5. The experiments with satellite radiance DA (i.e., EXP3 and 5) performed better than those without DA (i.e., EXP1 and 4). Thus, the effect of satellite radiance DA was important for both short-range (i.e., 25–30 h) and longer-range (25–48 h) forecasts. For the experiments using the same microphysics scheme, DA enhanced the forecast accuracy.

The time-averaged observation value of the SWD was 40.2 W m^{-2} (Fig. 2b). The time averaged SWD values of 25–30 h (25–48 h) forecasts in EXP1, 2, 3, 4, and 5 were 85.4, 84.0, 82.5, 73.6, and 70.6 (79.9, 80.4, and 78.3, 65.8 and 65.0) W m^{-2}, respectively. The overestimation of SWD in the model was improved the most in the 25–48 h forecasts of EXP5. Regardless of the forecast times, the experiments with Morrison (i.e., EXP4 and 5) performed better than the experiments with WSM5 (i.e., EXP1, 2, and 3). For the experiments using the same microphysics scheme, the experiments with DA (i.e., EXP2, 3, and 5) performed better than the experiments without DA (i.e., EXP1 and 4). The overestimation of the SWD was reduced more in the experiments with satellite radiance DA (i.e., EXP3 and 5) than that without satellite radiance DA (i.e., EXP2).

Because radiation fluxes in the PWRF are affected by the accuracy of cloud simulations, a smaller radiation flux error indicates an improvement in the cloud simulations. In general, EXP5 with the Morrison scheme and DA of the satellite radiance data in addition to the conventional observations showed the best performance in simulating the radiation fluxes.

In terms of dates, LWD distinctly decreased around September 6, 8–9, 13, and 17–18 (Fig. 2a). For LWD, Morrison performed better than WSM5 on September 6 and 13, whereas WSM5 performed better than Morrison on September 8–9 and 17–18 (Fig. 2a). Overall, SWD was simulated well when using Morrison rather than WSM5 (Fig. 2b).

Compared to observations, the LWD (SWD) forecasts for September 6 in all experiments rapidly decreased (increased). This rapid decrease (increase) of LWD (SWD) was reduced in the 25–48 h forecasts of all experiments except EXP1 (not shown), which implies that the radiation flux error reduced for longer forecast times and for the experiments with DA.

For September 8–9, LWD and SWD were simulated most accurately in EXP3 with WSM5, followed by EXP2 and EXP1 (Fig. 2a). When Morrison was used for September 8–9, the model biases of LWD and SWD increased.

On September 13, all experiments with WSM5 showed the start time of decreasing LWD as earlier than that of the observation and

overestimated the SWD. In contrast, the experiments with Morrison showed the start time of decreasing LWD more accurately and simulated more accurate SWD.

For September 17–18, LWD and SWD were simulated most accurately in EXP3, followed by EXP1 and 2. The LWD forecast in EXP1 was similar to that in EXP4, and the LWD forecast in EXP3 was more similar to observations than EXP5, which implies that the Morrison scheme was not effective at that time.

3.1.3. Relation with cloud fraction

Variations of the radiation flux are closely related to the cloud. To understand the effect of clouds on the radiation flux, the amount and type of clouds were analyzed. The cloud fraction (CF) at Hopen station was calculated using both the cloud liquid water path (CLWP) and cloud ice water path (CIWP) from the model simulation, as shown in Eq. (1) (Fogt and Bromwich, 2008; Wilson et al., 2012):

$$CF = 0.075*CLWP + 0.170*CIWP, \quad (1)$$

where the units of the CLWP and CIWP are kg m^{-2}, and that of the weightings (i.e., 0.075 and 0.170) is m^2 g^{-1}. Since the CF can fluctuate rapidly at some points in the time series, the CF was averaged for 5 h at every 3 h intervals (i.e., 03 UTC: average over 01–05 UTC, 06 UTC: average over 04–08 UTC, …), and the three hourly time-series data were used to analyze the general characteristics of the CF (Fig. 3a). The calculated CF values were generally less than 0.2, similar to that reported by Bromwich et al. (2013). As shown in Fig. 2, the cloud amount simulated in the model was insufficient. The dates at which the CF decreased (i.e., September 6, 8, 13–14, and 17–18) coincided with the dates when LWD and SWD changed rapidly.

The maxima of the CIWP and CLWP were near 500 and 950 hPa, respectively (not shown). Since the CIWP existed only for a few days (Fig. 3b), the clouds in the Arctic in the summer were mainly determined by low-level cloud liquid water (Fig. 3c). The increase of low-level CF over the ocean is related to active heat and moist flux interactions between the ocean and the atmosphere in the summer (Yeo et al., 2018). Wesslén et al. (2014) reported no cloud ice characteristics in the ASR, in contrast to ERA Interim reanalysis (ERA—I). In this study, the microphysics scheme had significant effects on both CIWP and CLWP (Fig. 3b and c). Especially at 00 UTC on September 16 and 00 UTC on September 17, the CIWP with WSM5 and Morrison were noticeably different (Fig. 3b). Since the CLWP is more closely associated with LWD and SWD, the large CF at 00 UTC on September 16 and 17 caused by large CIWP (Fig. 3a and b) was not related to large LWD and SWD (Fig. 2). As shown in Wilson et al. (2012), ice clouds are mainly formed during the night when the temperature drops, and thus have little effect on SWD and LWD at night (Fig. 2 and 3).

In the previous studies using the PWRF, the CLWP was simulated as 0–0.3 kg m^{-2} (mostly less than 0.2) (Bromwich et al., 2009) or 0–0.175 kg m^{-2} (mostly less than 0.1) (Hines et al., 2011) over the polar region in the summer, similar to the results in Fig. 3. On average, more CLWP was simulated with Morrison than with WSM5 (Fig. 3c). For September 6, 8, 13–14, and 17–18, as the amount of the CLWP from each experiment increased (Fig. 3c), more LWD and less SWD were simulated (Fig. 2). When the large differences of the CLWP between experiments appeared at 06 UTC on September 18, the CLWPs in EXP1, 2, 3, 4, and 5 were 0.014, 0.003, 0.050, 0, and 0.91 kg m^{-2}, respectively. At the same time, LWD (SWD) in EXP1, 2, 3, 4, 5, and the observation were 248.98, 249.93, 302.21, 250.93, 320.20, and 323.6 W m^{-2} (64.31, 64.29, 37.07, 54.81, 33.94, and 26.1 W m^{-2}), respectively. The CLWP was underestimated in EXP1, 2, and 4, whereas the underestimation of the CLWP was reduced in EXP3 and 5. Because of the more accurate CLWP simulations in EXP3 and 5, the LWD and SWD simulations in EXP3 and 5 were closer to the observations.

The cloud formation (i.e., CLWP and CIWP) could be affected by the water vapor in the atmosphere (Wesslén et al., 2014; Hines et al., 2019).

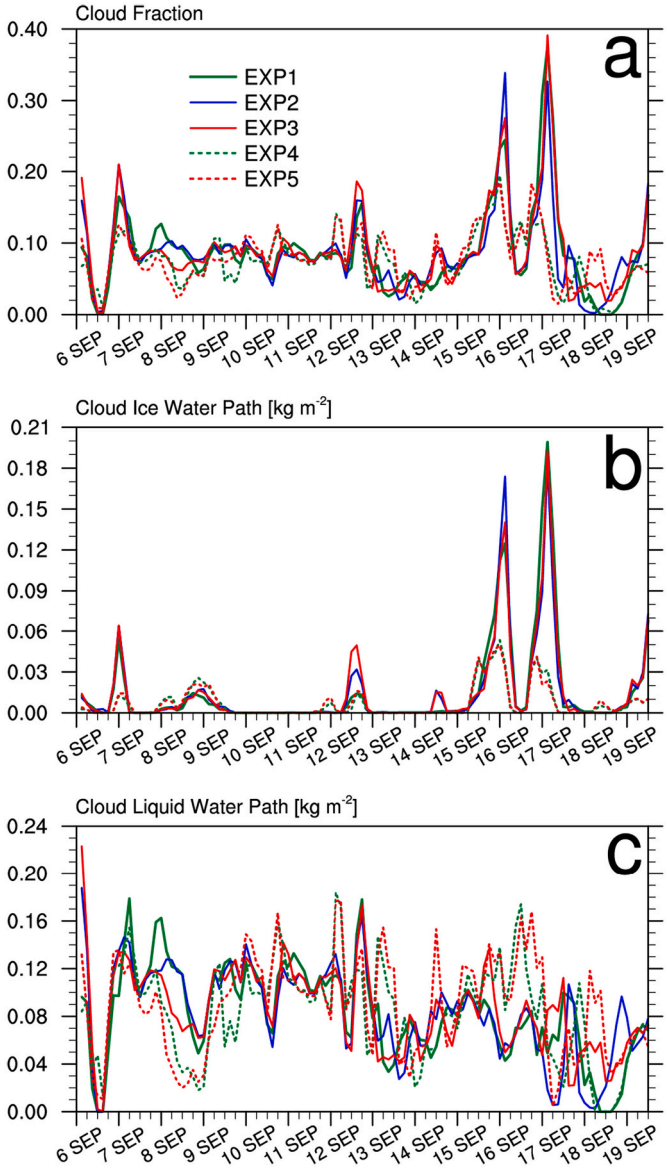

Fig. 3. Time series of the 25–30 h forecasts of EXP1, EXP2, EXP3, EXP4, and EXP5 for (a) cloud fraction, (b) cloud ice water path (kg m^{-2}), and (c) cloud liquid water path (kg m^{-2}).

The analyzed water vapor distributions at 00 UTC on September 17 are shown in Fig. 4. Fig. 4a–e show the vertically integrated water vapor analysis of EXP1, 2, 3, 4, and 5 at 00 UTC on September 17, respectively. The large water vapor was mainly located around the southwest of Svalbard in EXP1 (Fig. 4a), and the distributions of water vapor in EXP2 and 3 (Fig. 4b and c) were roughly consistent with that in EXP1 (Fig. 4a). Over the southeast of Svalbard, the amount of water vapor simulated in EXP3 was greater than that in EXP1 and 2 (Fig. 4f and g) and that in EXP5 was also greater than that in EXP4 (Fig. 4h).

The 30 h forecasts of the CLWP at 06 UTC on September 18 are shown in Fig. 5. Around the Hopen station (Fig. 1b), a small amount of the CLWP was simulated in EXP3 (Fig. 5c) and EXP5 (Fig. 5e), whereas no CLWP was shown in EXP1 (Fig. 5a), EXP2 (Fig. 5b), and EXP4 (Fig. 5d), which resulted in the difference in the radiation fluxes. The differences in the CLWP forecasts at 06 UTC on September 18 were caused by the differences in the analyses 30 h ahead (i.e., 00 UTC 17 SEP). Since the water vapor in the atmosphere could affect cloud formation, the changes in the distribution and amount of water vapor at the initial time (i.e., 00 UTC 17 SEP) could contribute to the simulation of

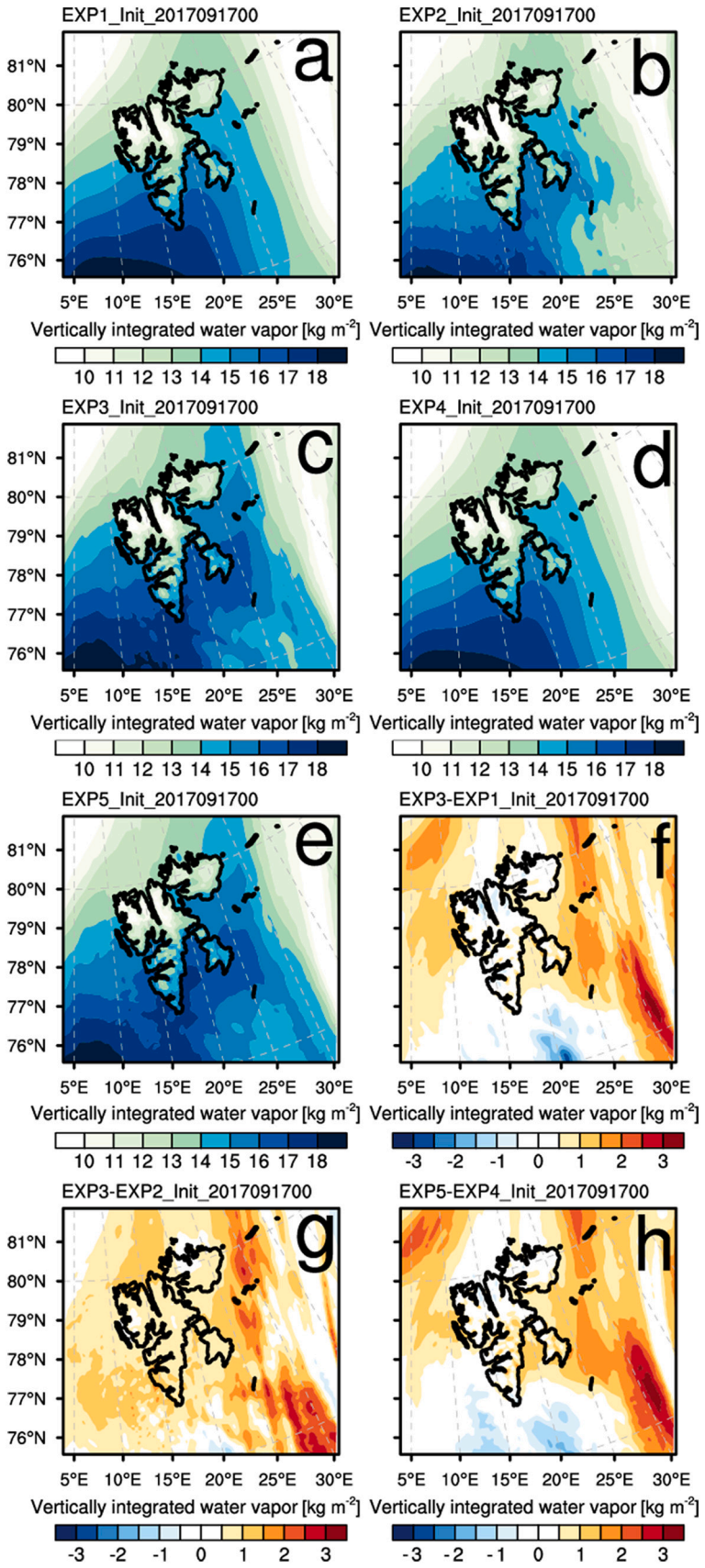

Fig. 4. Vertically integrated water vapor (shading, kg m^{-2}) at the analysis time (00 UTC 17 SEP 2017) in domain 3: (a) EXP1, (b) EXP2, (c) EXP3, (d) EXP4, (e) EXP5, (f) difference between EXP3 and EXP1, (g) difference between EXP3 and EXP2, and (h) difference between EXP5 and EXP4.

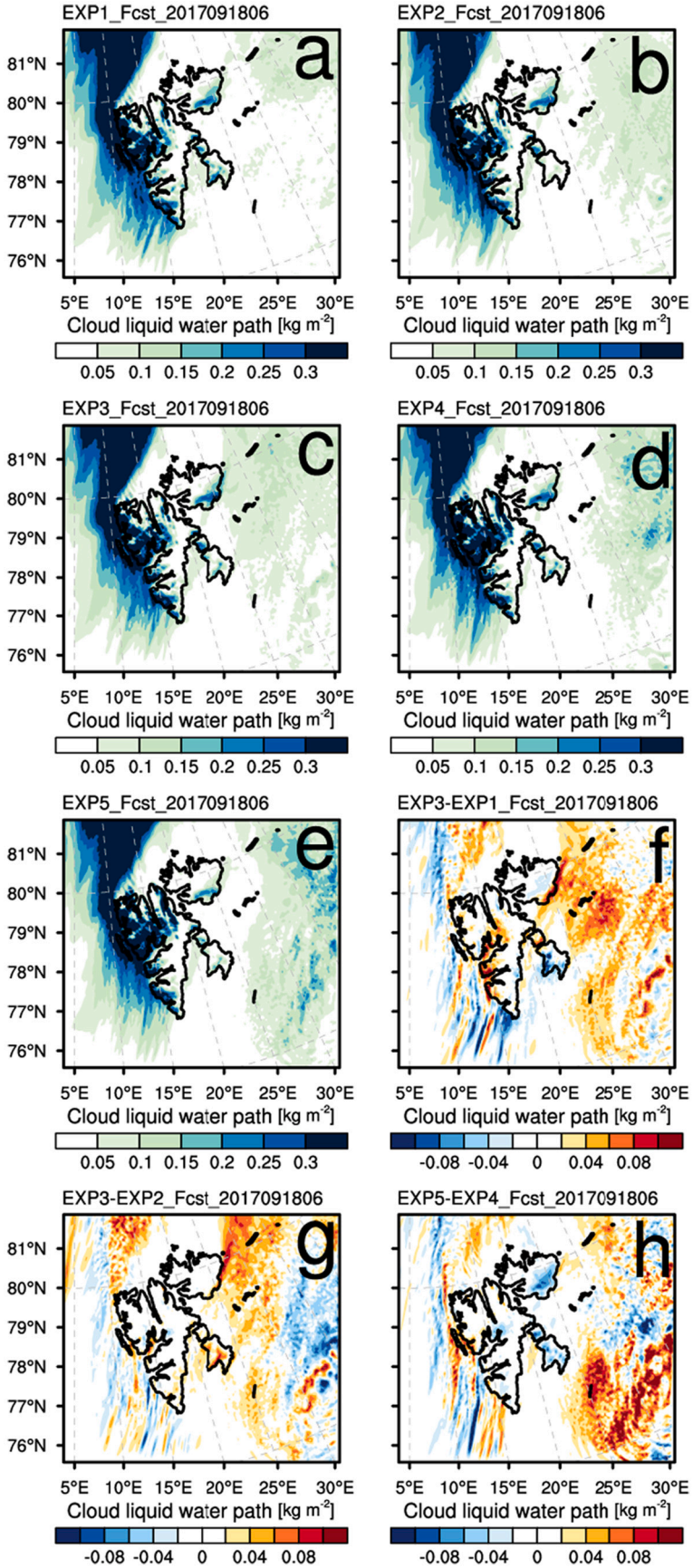

Fig. 5. The cloud liquid water path (shading, kg m^{-2}) at the 30 h forecast time (06 UTC 18 SEP 2017) in domain 3: (a) EXP1, (b) EXP2, (c) EXP3, (d) EXP4, (e) EXP5, (f) difference between EXP3 and EXP1, (g) difference between EXP3 and EXP2, and (h) difference between EXP5 and EXP4.

the CLWP 30 h later (i.e., 06 UTC 18 SEP). Thus, the 30 h forecasts of the CLWP in each experiment are different over the east of Svalbard (Fig. 5f–h).

When using WSM5, EXP3 simulated CLWP more than EXP2. EXP1 rarely simulates the CLWP. The difference in the CLWPs between EXP1 and 3 is thought to be associated with the water vapor difference at the initial time (i.e., 00 UTC 17 SEP), which is due to the additional assimilation of satellite data in EXP3. As the radiance data were assimilated at 00 UTC on September 17 in EXP3, the amount of water vapor in the initial condition increased over the east of Svalbard (Fig. 6a). The locations of large water vapor increments (Fig. 6a and b) over the east of Svalbard corresponded to the area where the MHS radiance data were assimilated (Fig. 6c). More CLWP was simulated in EXP4 over the east of Svalbard than in EXP1 (Fig. 5a and d), although both experiments have exactly the same water vapor conditions. This indicates that Morrison can simulate more clouds than WSM5.

In EXP5, which assimilated additional satellite data and used Morrison, more water vapor was analyzed over the east of Svalbard as compared to EXP4 (Fig. 4d, e, and h). Given more water vapor in the initial condition, Morrison further increased CLWP in EXP5 in the Hopen over the east of Svalbard (Fig. 5d, e, and h). Therefore, by using Morrison instead of WSM5 and assimilating satellite radiance data in addition to conventional data, more clouds could be simulated in the model. In addition, since the horizontal advection of clouds also plays an important role after the generation of clouds, the correction of the water vapor over a larger area in an initial condition has a positive influence on the CLWP simulations.

3.1.4. Relation with hydrometeors

Fig. 7 shows the vertical distributions of five hydrometeor species (i.e., water vapor (Qvapor), cloud liquid water (Qcloud), cloud ice water (Qice), snow (Qsnow), and rain (Qrain)) for domain 3 for EXP1 and 4, as well as the differences between the experiments (i.e., EXP2 – EXP1, EXP3 – EXP1, and EXP5 – EXP4) at 06 UTC on September 18. In EXP1 and 4, in which the same initial conditions were used at 00 UTC on September 17, the total amount of Qvapor integrated vertically up to 100 hPa and horizontally over domain 3 at the forecast time (06 UTC 18 SEP) in EXP1 and 4 were 9711 kg kg^{-1} and 9784 kg kg^{-1}, respectively (Fig. 7a). The differences are caused purely by the differences in the microphysics scheme. There were more Qcloud, Qice, Qsnow, and Qrain in EXP4 than in EXP1 for almost all vertical levels (Fig. 7b). In EXP2, the vertically and horizontally integrated total amount of Qvapor was similar to that in EXP1 (Fig. 7a), but the Qcloud increased slightly at certain low levels compared to that in EXP1 (Fig. 7c). Compared to EXP1 and 4, Qvapor increased in EXP3 and 5 at low levels, respectively (Fig. 7a). Compared with EXP1 (EXP4), the vertically and horizontally integrated total amounts of Qcloud, Qice, Qsnow, and Qrain in EXP3 (EXP5) were changed by 23.1, −5.4, −1.2, and 10.5% (12.9, 1.3, 1.0, and 8.1%), respectively. Therefore, DA contributed to the increase of the hydrometeor species at low levels, which is related to low-level clouds (Fig. 7b and d).

3.2. Effect of data assimilation and microphysics on surface heat flux

3.2.1. Bias and RMSE

Table 4 shows the bias and RMSE for the SHX and LHX forecasts in each experiment, against the observations at the Dasan station of the Republic of Korea over the Ny-ålesund in Svalbard. The positive (negative) heat flux indicates that the heat was transferred from the surface (atmosphere) to the atmosphere (surface). For all experiments, the SHX forecasts show a negative bias, and the LHX forecasts show a positive bias compared to the observations. In contrast to the error statistics of radiation (Table 3), the bias and RMSE of the 25–48 h forecasts were not smaller than those of the 25–30 h forecasts. The forecast error in EXP1 was reduced in EXP2 and 3. Compared to EXP1, the 25–30 h forecast error for SHX in EXP3 was reduced by 3.91% for

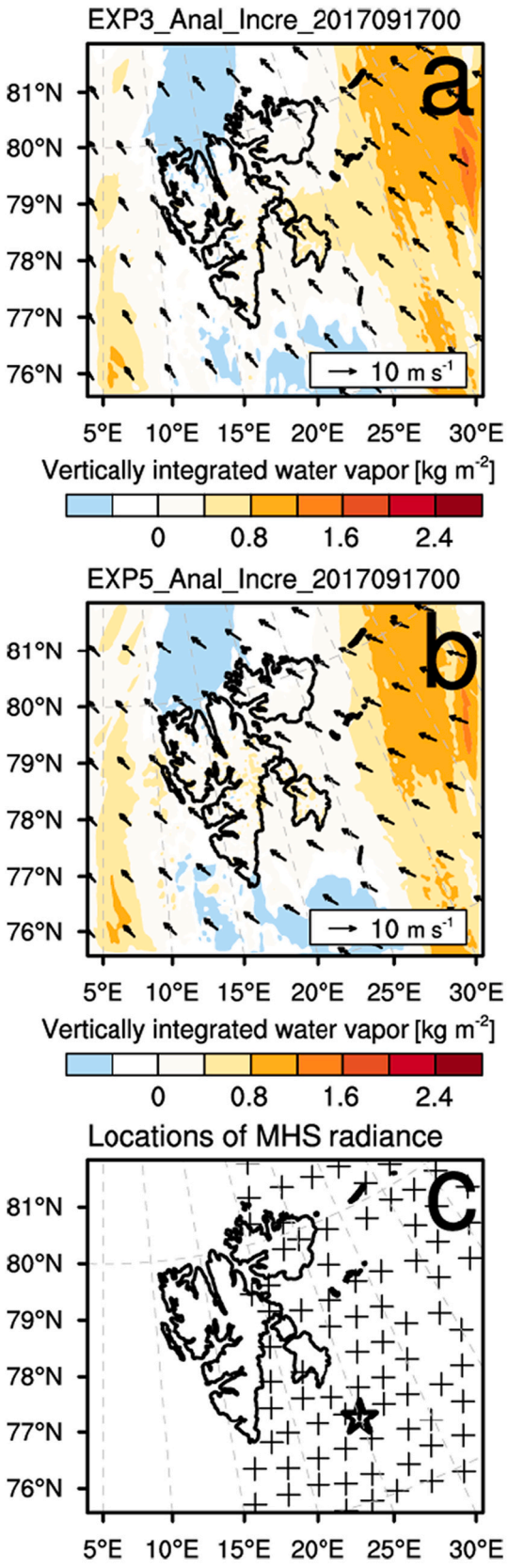

Fig. 6. The analysis increment for vertically integrated water vapor (shading, kg m^{-2}) and wind vector (m s^{-1}) at the analysis time (00 UTC 17 SEP 2017) in domain 3: (a) EXP3 and (b) EXP5. (c) The location of the Hopen radiation observation station (★) and that of satellite radiance observations (+) assimilated at the analysis time (00 UTC 17 SEP 2017).

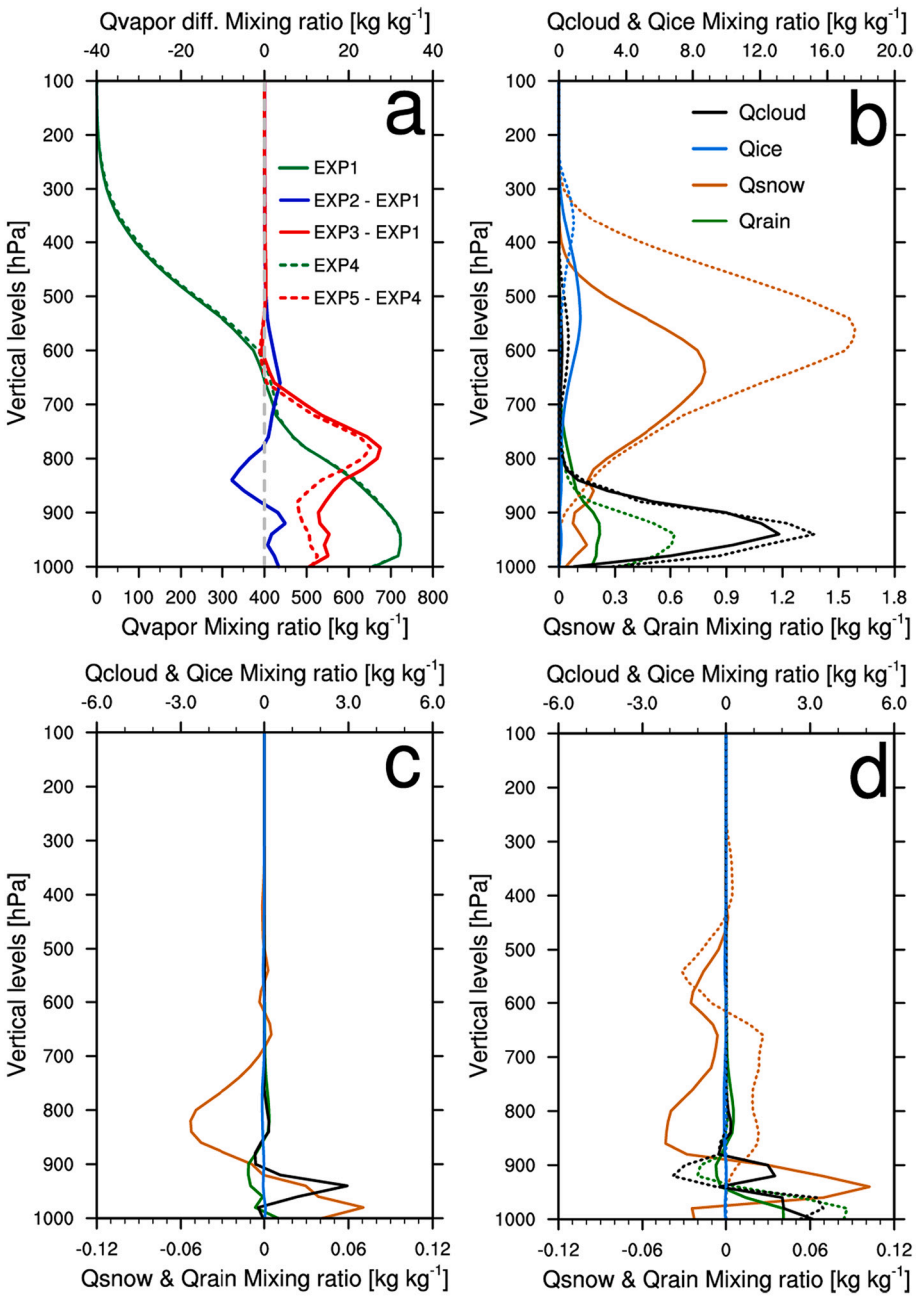

Fig. 7. (a) The vertical distribution of horizontally integrated water vapor (Qvapor) for domain 3 in EXP1 (EXP4) at 06 UTC 18 SEP 2017 and its differences in EXP2 and EXP3 (EXP5) against EXP1 (EXP4). (b) The vertical distributions of horizontally integrated hydrometeors (Qcloud, Qice, Qsnow, and Qrain) for domain 3 in EXP1 and EXP4 at 06 UTC 18 SEP 2017. The differences of vertical distributions for hydrometeors in (c) EXP2 against EXP1 and (d) EXP3 (EXP5) against EXP1 (EXP4). EXP1, 2, and 3 are denoted by solid lines, whereas EXP4 and 5 are denoted by dashed lines.

bias and 3.25% for RMSE, and the 25–30 h forecast error for LHX in EXP3 was reduced by 10.31% for bias and 7.80% for RMSE. The bias and RMSE in EXP4 (EXP5) were smaller than those in EXP1 (EXP3), which implies better performance of Morrison compared to WSM5 in heat flux forecasts. Compared to EXP4, the 25–30 h forecast error for SHX (LHX) in EXP5 was reduced by 4.08% (16.15%) for bias and 2.45% (3.09%) for RMSE. Thus, regardless of the microphysics schemes, DA reduced the bias and RMSE for the heat flux forecasts. In addition, regardless of the DA, the use of Morrison reduced the bias and RMSE for the heat flux forecasts compared to the WSM5. Therefore, using both DA and Morrison reduced the bias and RMSE of the heat flux forecasts the most.

As in previous studies (Bromwich et al., 2009; Hines et al., 2015) for the evaluation of the performance of the PWRF based on SHEBA observations, the bias of SHX is much greater than that of LHX, which is caused by the adjustment of SHX after LHX calculation to have the surface energy balance.

3.2.2. *Time series*

Fig. 8a and b shows the time series of the 25–30 h forecasts for each experiment and observations for SHX and LHX, respectively. The time-averaged observation values of SHX and LHX were − 14.70 and 19.09 W m^{-2} for the experimental period, which implies that the sensible (latent) heat moved from the atmosphere to surface (surface to the atmosphere). Compared to observations, the more sensible (latent) heat moved from the atmosphere to the surface (from the surface to the atmosphere) in the experiments. The time-averaged SHX values in EXP1, 2, 3, 4, and 5 were − 76.67, −74.68, −73.69, −76.02, and − 73.53 W m^{-2}. The time averaged LHX values in EXP1, 2, 3, 4, and 5 were 29.08, 27.70, 27.24, 27.32, and 25.45 W m^{-2}. Therefore, when using Morrison or assimilating satellite radiance data in addition to the conventional data, the heat flux simulations in the PWRF were more similar to observations.

The differences between the simulated LHXs were large at 18 UTC on September 6 (Fig. 8b). The LHX forecasts overestimated the observations

Table 4
Average forecast error statistics for the downward sensible and latent heat flux of each experiment and forecast time at the Dasan observation station of the Republic of Korea.

Variable	Experiment	25–30 h forecast		25–48 h forecast	
		Bias	RSME	Bias	RMSE
Sensible heat flux (W m^{-2})	EXP1	-62.006	77.515	-62.766	79.126
	EXP2	-59.934	75.286	-61.597	78.233
	EXP3	-59.581	74.998	-60.079	76.430
	EXP4	-61.473	76.098	-60.582	76.074
	EXP5	-58.967	74.233	-59.795	74.615
Latent heat flux (W m^{-2})	EXP1	11.394	39.259	12.671	37.797
	EXP2	10.215	35.682	11.071	36.273
	EXP3	10.219	36.197	10.019	36.129
	EXP4	10.418	36.772	9.864	34.438
	EXP5	8.736	35.634	9.262	33.449

The grey shadings in EXP2, 3, 4, and 5 denotes the Bias and RMSE which were smaller (i.e., improved) compared to those in EXP1.

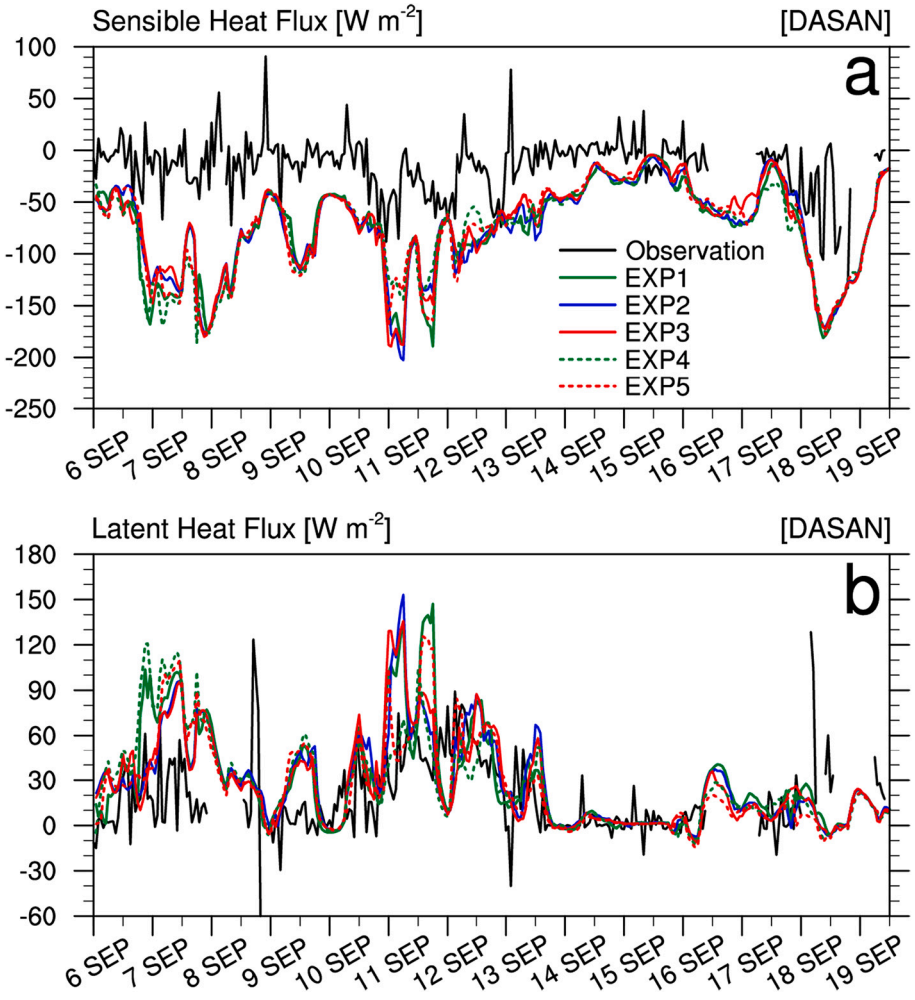

Fig. 8. Time series of observations and the 25–30 h forecasts of EXP1, EXP2, EXP3, EXP4, and EXP5 for (a) sensible heat flux (W m^{-2}) and (b) latent heat flux (W m^{-2}).

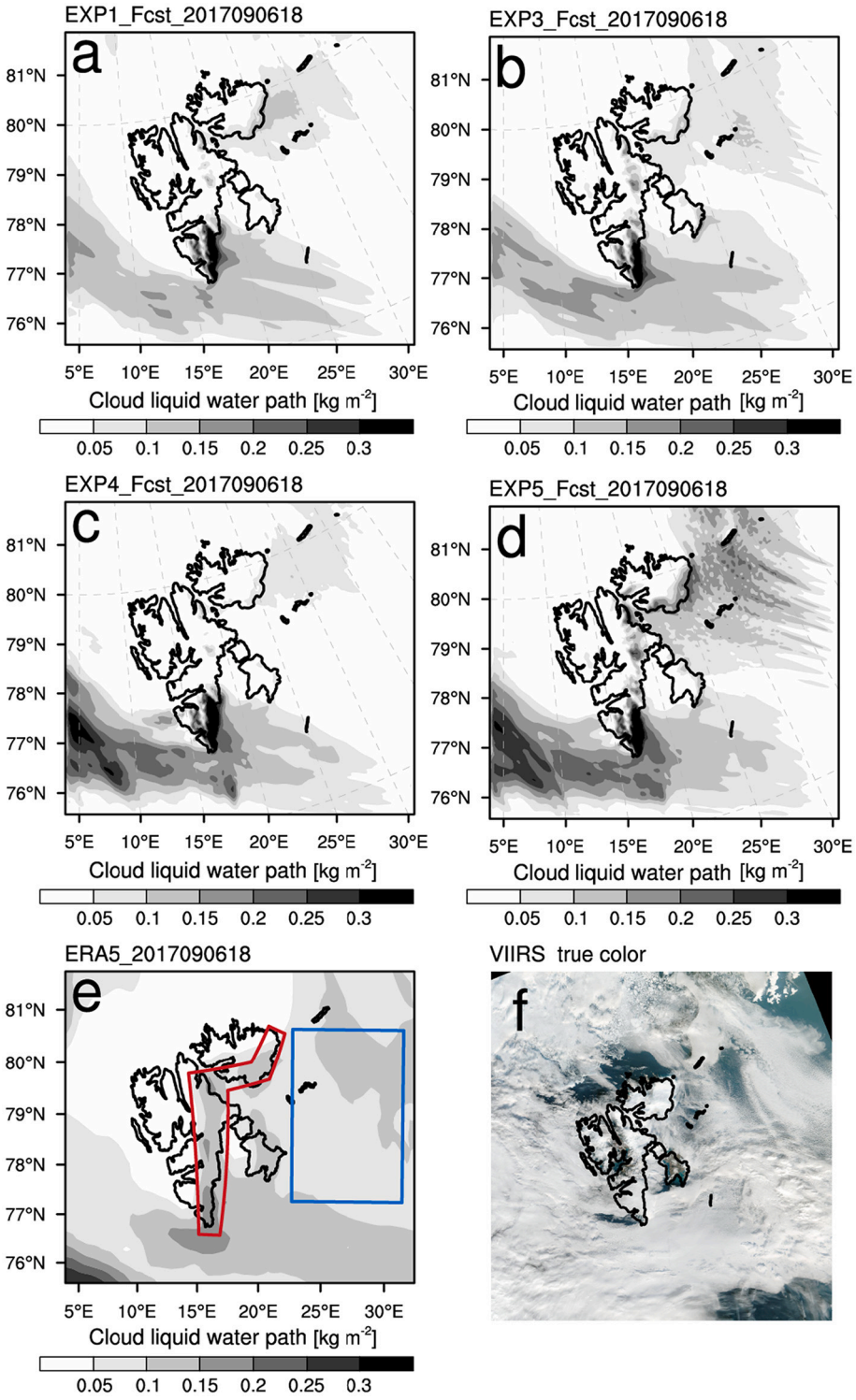

Fig. 9. The cloud liquid water path (kg m^{-2}) in domain 3: (a) EXP1, (b) EXP3, (c) EXP4, and (d) EXP5 at the 30 h forecast time (18 UTC 06 SEP 2017) and (e) ERA5 reanalysis at 18 UTC 06 SEP 2017. The red box and blue box in (e) indicate the land slope and eastern sea of Svalbard, respectively. (f) The VIIRS true color image at 10 UTC 06 SEP 2017. (For interpretation of the references to color in this figure legend, the reader is referred to the web version of this article.)

in the experiments without DA (i.e., EXP1 and 4), whereas LHX forecasts in the experiments with DA (i.e., EXP2, 3, and 5) were more similar to observations.

3.2.3. *Relation with cloud fraction*

The simulated CLWP distributions at 18 UTC on September 06 when large differences of heat flux forecasts existed between experiments are shown in Fig. 9. The distributions of the 30 h forecasts of CLWP in EXP1 and 4 without DA and EXP3 and 5 with DA were compared with those in ERA5 reanalysis and a true color composite image pictured by the Visible Infrared Imaging Radiometer Suite (VIIRS) sensor on the National Polar-orbiting Partnership (SNPP) satellite (www.sat.dundee.ac.uk) (Fig. 9). Note that there was a slight time difference between the ERA5 reanalysis (at 18 UTC 06 SEP) in Fig. 9e and the cloud pattern of

VIIRS (at 10 UTC 06 SEP) in Fig. 9f.

ERA5 simulated the clouds over the land slope and the eastern sea of Svalbard (Fig. 9e), which was close to the VIIRS image (Fig. 9f). The CLWP was underestimated in EXP1 and 4 over those regions (Fig. 9a and c). In contrast, more CLWP was simulated over those regions in EXP3 and 5 with satellite radiance DA (Fig. 9b and d). EXP5 simulated clouds most closely to the VIIRS image (Fig. 9d and f). Over the entire domain, the amounts of clouds were greater in the experiments using Morrison (i.e., EXP4 and 5) than those using WSM5 (i.e., EXP1 and 3). In general, the underestimation of clouds and the associated decrease of LWD and increase of SWD (Hines et al., 2011) are related to the biases of the SHX, LHX, and 2 m temperatures.

Fig. 10 compares the SHX, LHX, and 2 m temperatures at 18 UTC on September 06 in EXP1, 3, 5, and the ERA5 reanalysis. The SHX and LHX distributions in EXP1, 3, and 5 were similar to those in ERA5 over the western sea of Svalbard, but showed positive biases compared to those in ERA5 over the eastern sea of Svalbard (Fig. 10a–h). Compared to ERA5, the SHXs in EXP1, 3, and 5 showed negative biases on the land (Fig. 10a–d). In contrast, the LHXs in EXP1, 3, and 5 were similar to those in ERA5 on land (Fig. 10e–h). The distributions of 2 m temperature in EXP1, 3, and 5 slightly underestimated that in ERA5 (Fig. 10i–l).

The biases of SHX, LHX, and 2 m temperature in the PWRF compared to the ERA5 are associated with the effects of LWD and SWD variations on SHX, LHX, and 2 m temperature depending on the surface type. Over the sea, the effects of increased SWD are more important than those of decreased LWD. The decrease of LWD had little effect on the 2 m temperature variation owing to the high heat capacity of seawater. In contrast, the increase of SWD caused extra energy to accumulate on the sea surface owing to the low albedo. That extra energy was then balanced by generating more heat flux from the sea surface to the atmosphere. Accordingly, SWD increased over the eastern sea of Svalbard where less CLWP was simulated, which resulted in the increase of SHX and LHX in EXP1, 3, and 5 compared to the ERA5 (Fig. 9 and 10). Since the CLWP over the eastern sea of Svalbard was simulated the greatest in EXP5 compared to EXP1 and 3 (Fig. 9a, b, and d), the overestimations of SHX and LHX over the region were reduced the most in EXP5 compared to EXP1 and 3 (Fig. 10a–h).

Over land, the effects of decreased LWD were more important than

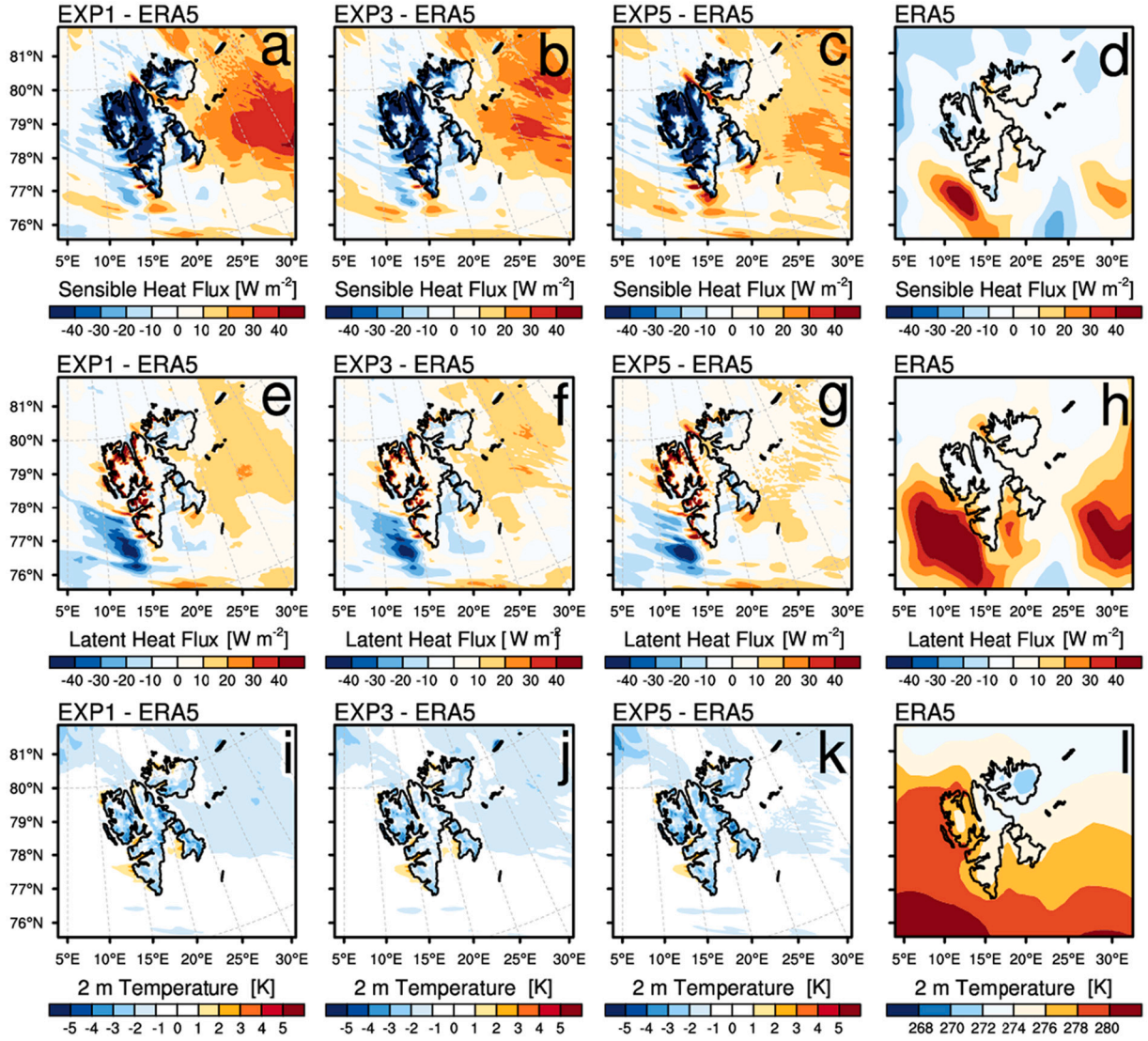

Fig. 10. The sensible heat flux (W m^{-2}) in domain 3: (a) difference between EXP1 and ERA5, (b) difference between EXP3 and ERA5, (c) difference between EXP5 and ERA5, and (d) ERA5 reanalysis at 18 UTC 06 SEP 2017. The latent heat flux (W m^{-2}): (e) difference between EXP1 and ERA5, (f) difference between EXP3 and ERA5, (g) difference between EXP5 and ERA5, and (h) ERA5 reanalysis at 18 UTC 06 SEP 2017. The 2 m temperature (K): (i) difference between EXP1 and ERA5, (j) difference between EXP3 and ERA5, (k) difference between EXP5 and ERA5, and (l) ERA5 reanalysis at 18 UTC 06 SEP 2017. EXP1, EXP3, and EXP5 are 30 h forecasts at 18 UTC 06 SEP 2017.

those of increased SWD. The increased SWD had little effect on the 2 m temperature variation due to the high albedo of the land. In contrast, the decrease of LWD caused a decrease of the 2 m temperature on the land owing to the low heat capacity. The sensible heat moved from the atmosphere to the surface (Fig. 10a–c). Based on ERA5, the average biases of the 2 m temperature in EXP1 and 3 were − 1.11 and − 1.04 K, respectively, on the land at 18 UTC on September 6, which was caused by the CLWP existing over a larger area in EXP3 as compared to EXP1. Compared to ERA5, the average biases of SHX and LHX on the land were − 23.31 W m^{-2} and 1.08 W m^{-2} in EXP1 and − 19.77 W m^{-2} and 0.08 W m^{-2} in EXP3. The average biases of the 2 m temperature, SHX, and LHX in EXP5 were − 1.27 K, −18.46 W m^{-2}, and 2.02 W m^{-2} against ERA5, respectively. Although the distribution and amount of the CLWP in EXP5 were similar to those in EXP3 on the land (Fig. 9b and d), the forecast errors of 2 m temperature and LHX in EXP5 were greater than those in EXP3, which implies that the WSM5 is better than Morrison in simulating 2 m temperature and LHX on the land. This is because the heat flux and 2 m temperature on the land are affected by near-surface meteorological variables as well as clouds.

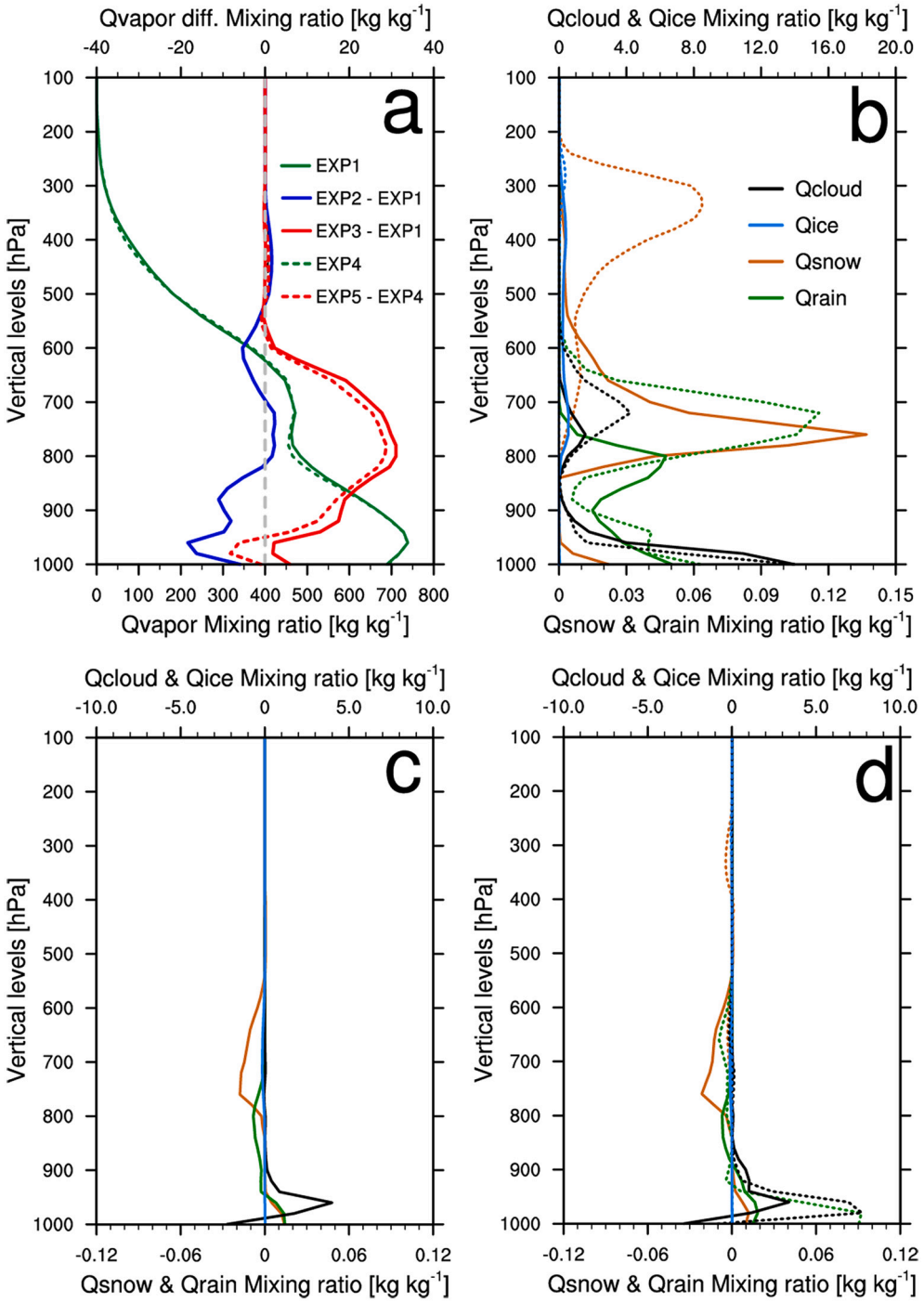

Fig. 11. (a) The vertical distribution of horizontally integrated water vapor (Qvapor) for domain 3 in EXP1 (EXP4) at 18 UTC 06 SEP 2017 and its differences in EXP2 and EXP3 (EXP5) against EXP1 (EXP4). (b) The vertical distributions of horizontally integrated hydrometeors (Qcloud, Qice, Qsnow, and Qrain) for domain 3 in EXP1 and EXP4 at 18 UTC 06 SEP 2017. The differences of vertical distributions for hydrometeors in (c) EXP2 against EXP1 and (d) EXP3 (EXP5) against EXP1 (EXP4).

3.2.4. Relation with hydrometeors

Fig. 11 shows the vertical distributions of hydrometeor species for domain 3 for EXP1 and 4, and the differences between experiments at 18 UTC on September 06. In EXP1 and 4, with the same initial conditions, the vertically and horizontally integrated total amount of Qvapor in EXP1 (i.e., 9356 kg kg^{-1}) was greater than that in EXP4 (i.e., 9317 kg kg^{-1}) (Fig. 11a), whereas Qcloud (Qrain) was greater in EXP4 at mid- (mid- and lower) levels compared to EXP1 (Fig. 11b). Although the vertically and horizontally integrated total amount of Qvapor in EXP2 was less than that in EXP1 (Fig. 11a), the Qcloud in EXP2 increased slightly at low levels compared to that in EXP1 (Fig. 11c). Compared to EXP1 and 4, Qvapor increased in EXP3 and 5, respectively, which led to an increase of Qcloud and Qrain at low levels. Therefore, DA increased clouds in model simulations (Fig. 11b and d), and Morrison simulated more low-level clouds compared to WSM5 (Fig. 11b and d).

3.3. Effect of data assimilation and microphysics on near surface temperature, wind, and pressure

Table 5 shows the average bias and RMSE of the 25–30 h and 25–48 h forecasts for 10 m wind, 2 m temperature, and sea level pressure based on SYNOP observations over Svalbard. The forecast differences and forecast error differences between the experiments decreased as the forecast time increased. The forecast errors were smaller for the experiments with WSM5 than for those with Morrison. Positive wind biases appeared in all experiments, regardless of the forecast time. The DA reduced these positive wind biases; thus, the RMSEs for wind in EXP2 and 3 (EXP5) were smaller than those in EXP1 (EXP4). Negative temperature biases appeared in all experiments, which resulted from the underestimation of LWD, as in Bromwich et al. (2013) and Seo and Yang (2013). The DA reduced these negative temperature biases, especially for the 25–48 h forecasts; thus, the RMSEs for temperature in EXP2 and 3 (EXP5) were smaller than those in EXP1 (EXP4). Compared to wind and temperature, the DA effect was not clearly shown in the pressure forecasts. The experiments without DA (i.e., EXP1 and 4) using ERA5 as the initial condition generally showed smaller biases and RMSEs for pressure than the experiments with DA (i.e., EXP2, 3, and 5), which may be related to the better constraint of the larger-scale variable (i.e., pressure) when using the initial condition from the global reanalysis system (i.e., ERA5).

Fig. 12 presents the bias and RMSE of the forecasts for EXP1, 3, 4, and 5 at each observation station. Positive wind biases appeared at most of the stations, and the biases and RMSEs were smaller in EXP3 (EXP5) compared to EXP1 (EXP4), owing to the DA effect (Fig. 12a and b). The negative biases of temperature forecasts appeared at all stations in EXP1 and 4. These negative biases and the corresponding RMSE in EXP1 (EXP4) were improved in EXP3 (EXP5) at most stations (Fig. 12c and d). Both positive and negative biases of pressure forecasts appeared depending on the stations, showing biases of less than 1 hPa for most of the stations. Overall, DA in combination with WSM5, rather than Morrison, reduced the forecast errors for near-surface meteorological variables.

4. Summary and discussion

In this study, the effect of assimilating conventional observations and satellite radiance data around Svalbard on forecasts was analyzed by comparing the forecasts of the experiment without DA using the ERA5 reanalysis as the initial conditions and those of the experiment with DA using the initial conditions from the analysis-forecast system with a 3DVAR method. PWRF was used as the forecast model. In addition, the effects of two microphysics schemes, WSM5 and 2-moment Morrison, on the forecasts over Svalbard were analyzed. The experiments were conducted for September 1–19, 2017. Near-surface observations for meteorological variables (i.e., 10 m wind speed, 2 m temperature, and sea level pressure) and radiation observations over Svalbard, including heat flux observations at Dasan station, were used to verify the forecasts.

All experiments underestimated (overestimated) the LWD (SWD) compared to observations for the entire period. This is because the thin clouds which were consistently present at low levels in the summer over Svalbard were not sufficiently simulated in the model. When the cloud amount was reduced in the model, the forecast errors of the radiation

Table 5
Average forecast error statistics for the wind (highest 10 min. average wind for the last 1 h), temperature, and pressure of each experiment and forecast time at all verification observation stations.

Variable	Experiment	25–30 h forecast		25–48 h forecast	
		Bias	RSME	Bias	RMSE
Wind ($m\ s^{-1}$)	EXP1	0.834	2.901	0.787	2.876
	EXP2	0.810	2.852	0.740	2.864
	EXP3	0.752	2.853	0.705	2.851
	EXP4	0.855	2.935	0.862	2.931
	EXP5	0.795	2.896	0.779	2.923
Temperature (K)	EXP1	-1.233	1.814	-1.279	1.907
	EXP2	-1.266	1.829	-1.265	1.904
	EXP3	-1.213	1.806	-1.249	1.902
	EXP4	-1.249	1.849	-1.306	1.950
	EXP5	-1.272	1.846	-1.301	1.936
Pressure (hPa)	EXP1	-0.053	1.010	0.053	1.317
	EXP2	-0.074	1.015	0.022	1.317
	EXP3	-0.141	1.048	-0.010	1.321
	EXP4	-0.128	1.047	-0.024	1.352
	EXP5	-0.188	1.080	-0.072	1.353

The grey shadings in EXP2, 3, 4, and 5 denotes the Bias and RMSE which were smaller (i.e., improved) compared to those in EXP1.

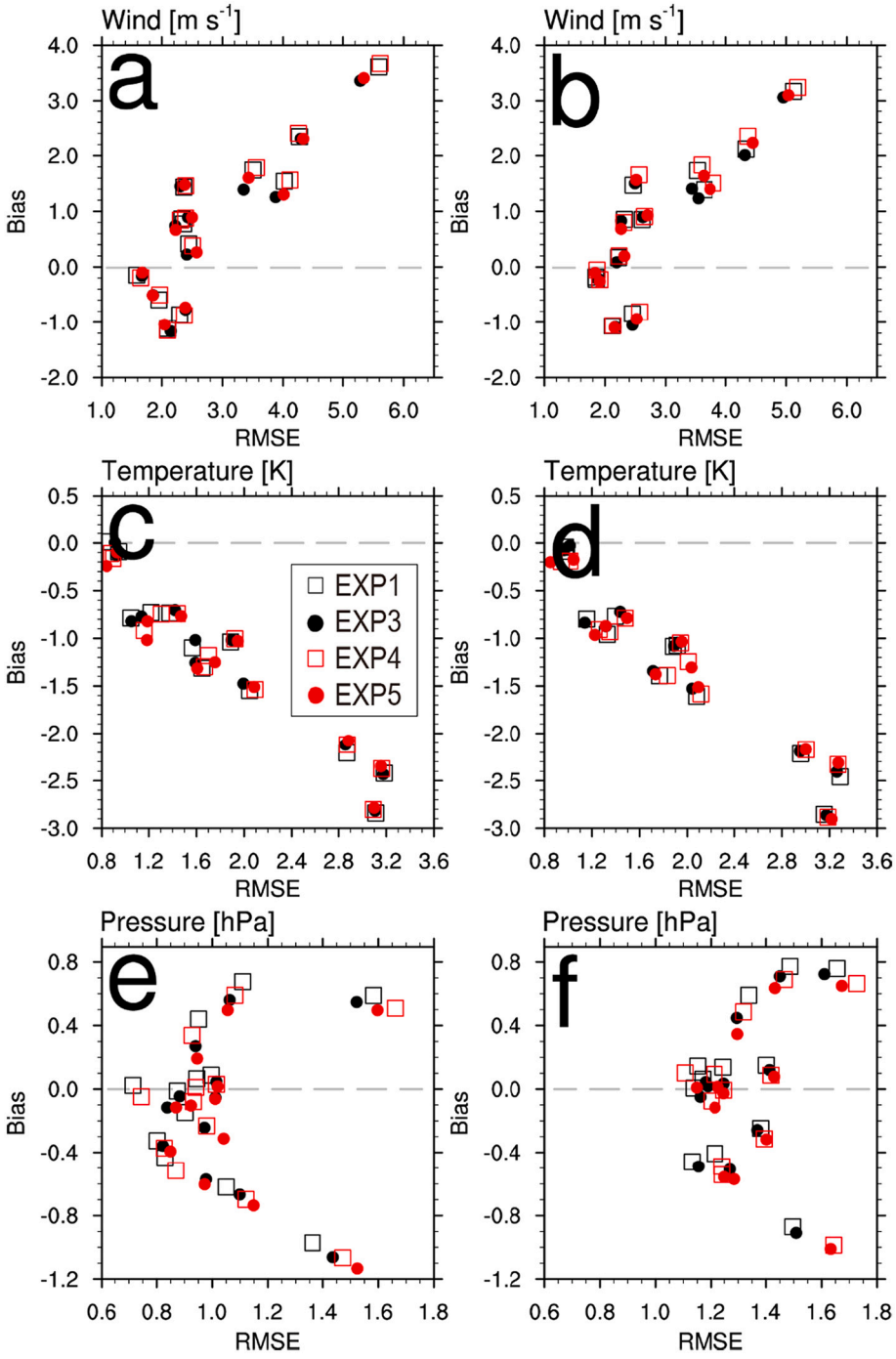

Fig. 12. The diagrams for RMSE and Bias of (a), (c), (e) the 25–30 h forecasts and (b), (d), (f) 25–48 h forecasts for wind, temperature, and pressure in EXP1, EXP3, EXP4, and EXP5.

fluxes increased rapidly. Moreover, because the differences in the cloud ice (liquid) water path between experiments were small (large), the Arctic cloud was mainly affected by the cloud liquid water in the summer.

At the analysis time, the amount of water vapor in EXP2, which used only conventional observation DA, was less than that in ERA5. In contrast, the amount of water vapor in EXP3 and 5 with both conventional observations and satellite radiance data DA was slightly higher than that in ERA5. Because of the increase in water vapor, more CLWP was simulated, and the RMSEs of the 25–30 h forecasts for LWD and SWD in EXP3 (EXP5) were reduced by 12.7% and 8.1% (17.1% and 4.7%), respectively, compared to EXP1 (EXP4). In addition, the RMSEs of the 25–30 h forecasts for LWD and SWD in EXP4 with the 2-moment Morrison reduced by 4.2% and 25.8%, respectively, compared to those in EXP1 with WSM5. The RMSEs in EXP5 with the 2-moment Morrison and satellite radiance DA were reduced by 20.6% and 29.3%, respectively, compared to those in EXP1. Therefore, the experiment assimilating satellite radiance data and using the 2-moment Morrison simulated more CLWP, which resulted in the reduction of the forecast error of the radiation flux.

In terms of the sensible and latent heat flux, all experiments underestimated (overestimated) the SHX (LHX) compared to the observations. On the land, more SHX (LHX) from the atmosphere to the surface (from surface to atmosphere) was simulated in the model, compared to the

observations. The underestimation of clouds decreased the LWD, which in turn decreased the 2 m temperature on the land. The 2 m temperature on the land simulated in the PWRF was much lower than that in ERA5.

Because there are no heat flux observations over the ocean, the forecasts for heat fluxes and 2 m temperature in the experiments were compared with those in ERA5. Over the sea, the underestimation of clouds decreased the LWD, but the 2 m temperature decreased very little. However, the underestimation of clouds increased the SWD, which in turn increased the relative energy accumulation on the sea surface owing to the low albedo. This energy accumulation increased both SHX and LHX from the sea surface to the atmosphere. In some cases, the cloud distribution in the PWRF was more similar to that in the true color image of the VIIRS sensor than that in ERA5. Overall, the heat flux forecast errors decreased more with 2-moment Morrison than with WSM5. On average, the bias and RMSE of the 25–30 h forecasts for SHX and LHX in EXP3 (EXP5) were reduced by 3.25% and 7.80% (4.23% and 9.23%, respectively) compared to EXP1.

In contrast to the forecast accuracies for radiation and heat fluxes, the forecast accuracy for near-surface meteorological variables in the DA experiment with WSM5 was better than that with 2-moment Morrison. As more observations were assimilated, the forecast accuracies for 10 m wind speed and 2 m temperature were improved at most of the observation stations, compared to the experiment without DA. In contrast, the forecast error for sea level pressure with DA was greater than that without DA.

In summary, the 2-moment Morrison improved the forecast accuracies for radiation and heat fluxes at the surface by simulating more clouds than WSM5. However, the forecast accuracies for near-surface meteorological variables were better in the experiments with the WSM5 than with the 2-moment Morrison. For the radiation flux, heat flux, and near-surface variables, the forecast accuracies in the experiment with only conventional observations DA were comparable to or better than the experiment with ERA5 as the initial condition. The forecast accuracies in the experiments that assimilated both conventional observations and radiance data were distinctly improved compared to the experiments without DA. These results imply that the limitation of the cloud microphysics scheme in simulating the Arctic could be improved by assimilating satellite radiance data. To further enhance predictability over the Arctic region, studies on appropriate assimilation methods for various satellite data and observation impacts for forecasts need to be performed.

Declaration of Competing Interest

The authors declare that they have no known competing financial interests or personal relationships that could have appeared to influence the work reported in this paper.

Acknowledgments

The authors appreciate the reviewers' valuable comments. This study was supported by a National Research Foundation of Korea (NRF) grant funded by the South Korean government (Ministry of Science and ICT) (Grant 2021R1A2C1012572) and the Yonsei Signature Research Cluster Program of 2021 (2021-22-0003). The simulations were primarily conducted using the supercomputer system supported by the National Center for Meteorological Supercomputer of the Korea Meteorological Administration (KMA). The authors appreciate the Byrd Polar Research Center at Ohio State University for providing the Polar WRF model, the Korea Polar Research Institute for providing heat flux data, and the Norwegian Meteorological Institute for providing observation data through the eKlima site.

References

Bromwich, D.H., Hines, K.M., Bai, L.-S., 2009. Development and testing of polar weather research and forecasting model: 2. Arctic Ocean. J. Geophys. Res.-Atmos. 114, D08122.

Bromwich, D.H., Otieno, F.O., Hines, K.M., Manning, K.W., Shilo, E., 2013. Comprehensive evaluation of polar weather research and forecasting model performance in the Antarctic. J. Geophys. Res.-Atmos. 118, 274–292.

Bromwich, D.H., Wilson, A.B., Bai, L.-S., Moore, G.W.K., Bauer, P., 2016. A comparison of the regional Arctic System Reanalysis and the global ERA-Interim Reanalysis for the Arctic. Q. J. R. Meteorol. Soc. 142, 644–658.

Bromwich, D.H., Wilson, A.B., Bai, L., Liu, Z., Barlage, M., Shih, C.-F., Maldonado, S., Hines, K.M., Wang, S.-H., Woollen, J., Kuo, B., Lin, H.-C., Wee, T.-K., Serreze, M.C., Walsh, J.E., 2018. The arctic system reanalysis, version 2. Bull. Am. Meteorol. Soc. 99, 805–828. https://doi.org/10.1175/BAMS-D-16-0215.1.

Chen, F., Mitchell, K.E., Schaake, J., Xue, Y., Pan, H.-L., Koren, V., Duan, Q.Y., Ek, M., Betts, A., 1996. Modeing of land-surface evaporation by four schemes and comparison with FIFE observations. J. Geophys. Res.-Atmos. 101, 7251–7268.

Cohen, J., Screen, J.A., Furtado, J.C., Barlow, M., Whittleston, D., Coumou, D., Francis, J., Dethloff, K., Entekhabi, D., Overland, J., Jones, J., 2014. Recent Arctic amplification and extreme mid-latitude weather. Nat. Geosci. 7, 627–637.

Fogt, R.L., Bromwich, D.H., . Atmospheric moisture and cloud cover characteristics forecast by AMPS. Weather Forecast. 23, 914–930.

Francis, J.A., Vavrus, S.J., 2012. Evidence linking Arctic amplification to extreme weather in mid-latitudes. Geophys. Res. Lett. 39, L06801. https://doi.org/10.1029/2012GL051000.

Francis, J.A., Chan, W., Leathers, D.J., Miller, J.R., Veron, D.E., 2009. Winter Northern Hemisphere weather patterns remember summer Arctic Sea-ice extent. Geophys. Res. Lett. 36, L07503. https://doi.org/10.1029/2009GL037274.

Grell, G.A., Dévényi, D., 2002. A generalized approach to parameterizing convection combining ensemble and data assimilation techniques. Geophys. Res. Lett. 29, 38–1–38–4. https://doi.org/10.1029/2002GL015311.

Hines, K.M., Bromwich, D.H., 2008. Development and testing of Polar Weather Research and Forecasting (WRF) model. Part I: greenland ice sheet meteorology. Mon. Weather Rev. 136, 1971–1989.

Hines, K.M., Bromwich, D.H., 2017. Simulation of Late Summer Arctic Clouds during ASCOS with Polar WRF. Mon. Weather Rev. 145, 521–541.

Hines, K.M., Bromwich, D.H., Bai, L.-S., Barlage, M., Slater, A.G., 2011. Development and testing of Polar WRF. Part III: Arctic land. J. Clim. 24, 26–48.

Hines, K.M., Bromwich, D.H., Bai, L., Bitz, C.M., Powers, J.G., Manning, K.W., 2015. Sea ice enhancements to polar WRF. Mon. Weather Rev. 143, 2363–2385.

Hines, K.M., Bromwich, D.H., Wang, S.-H., Silber, I., Verlinde, J., Lubin, D., . Microphysics of summer clouds in central West Antarctica simulated by polar WRF and AMPS. Atmos. Chem. Phys. 19, 12431–12454. https://doi.org/10.5194/acp-19-12431-2019.

Hines, K.M., Bromwich, D.H., Silber, I., Russell, L.M., Bai, L., 2021. Predicting frigid mixed-phase clouds for pristine coastal Antarctica. J. Geophys. Res.-Atmos. 126 e2021JD035112.

Hong, S.-Y., Dudhia, J., Chen, S.-H., 2004. A revised approach to ice-microphysical processes for the bulk parameterization of cloud and precipitation. Mon. Weather Rev. 132, 103–120.

Iacono, M.J., Delamere, J.S., Mlawer, E.J., Shephard, M.W., Clough, S.A., Collins, W.D., 2008. Radiative forcing by long-lived greenhouse gases: calculations with the AER radiative transfer models. J. Geophys. Res.-Atmos. 113, D13103.

Intrieri, J.M., Fairall, C.W., Shupe, M.D., Persson, P.O.G., Andreas, E.L., Guest, P.S., Moritz, R.E., 2002. An annual cycle of Arctic surface cloud forcing at SHEBA. J. Geophys. Res.-Oceans 107 (C10), 8039. https://doi.org/10.1029/2000JC000439.

Janjic, Z.I., 1994. The step-mountain eta coordinate model: further developments of the convection, viscous sublayer and turbulence closure schemes. Mon. Weather Rev. 122, 927–945.

Jung, T., et al., 2016. Advancing polar prediction capabilities on daily to seasonal time scales. Bull. Am. Meteorol. Soc. 97, 1631–1647.

Kim, D.-H., Kim, H.M., Hong, J., 2019. Evaluation of wind forecasts over Svalbard using the high-resolution Polar WRF with 3DVAR. Arct. Antarct. Alp. Res. 51, 471–489. https://doi.org/10.1080/15230430.2019.1676939.

Loewe, K., Ekman, A.M.L., Paukert, M., Sedlar, J., Tjernström, M., Hoose, C., 2017. Modelling micro- and macrophysical contributors to the dissipation of an Arctic mixed-phase cloud during the Arctic Summer Cloud Ocean Study (ASCOS). Atmos. Chem. Phys. 17, 6693–6704.

Lubin, D., et al., 2020. AWARE: the atmospheric radiation measurement (ARM) West Antarctic radiation experiment. Bull. Am. Meteorol. Soc. 101, E1069–E1091.

Monin, A.S., Obukhov, A.M., 1954. Basic laws of turbulent mixing in the surface layer of the atmosphere. Tr. Akad. Nauk SSSR Geophiz. Inst. 24, 163–187.

Morrison, H., Milbrandt, J.A., 2015. Parameterization of cloud microphysics based on the prediction of bulk ice particle properties. Part I: scheme description and idealized tests. J. Atmos. Sci. 72, 287–311. https://doi.org/10.1175/JAS-D-14-0065.1.

Morrison, H., Curry, J.A., Khvorostyanov, V.I., 2005. A new double-moment microphysics parameterization for application in cloud and climate models. Part I: description. J. Atmos. Sci. 62, 1665–1677.

Overland, J.E., Wang, M., 2010. Large-scale atmospheric circulation changes are associated with the recent loss of Arctic Sea ice. Tellus A 62, 1–9. https://doi.org/10.1111/j.1600-0870.2009.00421.x.

Overland, J.E., Dethloff, K., Francis, J.A., Hall, R.J., Hanna, E., Kim, S.-J., Screen, J.A., Shepherd, T.G., Vihma, T., 2016. Nonlinear response of mid-latitude weather to the changing Arctic. Nat. Clim. Chang. 6, 992–999. https://doi.org/10.1038/nclimate3121.

Parrish, D.F., Derber, J.C., 1992. The National Meteorological Center's spectral statistical-interpolation analysis system. Mon. Weather Rev. 120, 1747–1763.
Randriamampianina, R., Schyberg, H., Mile, M., 2019. Observing system experiments with an Arctic mesoscale numerical weather prediction model. Remote Sens. 11, 981. https://doi.org/10.3390/rs11080981.
Semmler, T., McGrath, R., Wang, S., 2012. The impact of Arctic Sea ice on the Arctic energy budget and on the climate of the Northern mid-latitudes. Clim. Dyn. 39, 2675–2694. https://doi.org/10.1007/s00382-012-1353-9.
Seo, H., Yang, J., 2013. Dynamical response of the Arctic atmospheric boundary layer process to uncertainties in sea-ice concentration. J. Geophys. Res.-Atmos. 118, 383–402.
Sotiropoulou, G., Tjernström, M., Sedlar, J., Achtert, P., Brooks, B.J., Brooks, I.M., Persson, P.O.G., Prytherch, J., Salisbury, D.J., Shupe, M.D., Johnston, P.E., Wolfe, D., 2016. Atmospheric conditions during the Arctic Clouds in Summer Experiment (ACSE): contrasting open water and sea ice surfaces during melt and freeze-up seasons. J. Clim. 29, 8721–8744.
Thompson, G., Eidhammer, T., 2014. A study of aerosol impacts on clouds and precipitation development in a large winter cyclone. J. Atmos. Sci. 71, 3636–3658. https://doi.org/10.1175/JAS-D-13-0305.1.
Tjernström, M., et al., 2014. The Arctic Summer Cloud Ocean Study (ASCOS): overview and experimental design. Atmos. Chem. Phys. 14, 2823–2869.
Uttal, T., et al., 2002. Surface heat budget of the Arctic Ocean. Bull. Am. Meteorol. Soc. 83, 255–275.
Wesslén, C., Tjernström, M., Bromwich, D.H., de Boer, G., Ekman, A.M.L., Bai, L.-S., Wang, S.-H., 2014. The Arctic summer atmosphere: an evaluation of reanalysis using ASCOS data. Atmos. Chem. Phys. 14, 2605–2624.
Wilson, A.B., Bromwich, D.H., Hines, K.M., 2011. Evaluation of Polar WRF forecasts on the Arctic System Reanalysis domain: surface and upper air analysis. J. Geophys. Res.-Atmos. 116, D11112.
Wilson, A.B., Bromwich, D.H., Hines, K.M., 2012. Evaluation of Polar WRF forecasts on the Arctic System Reanalysis Domain: 2. Atmospheric hydrologic cycle. J. Geophys. Res.-Atmos. 117, D04107. https://doi.org/10.1029/2011JD016765.
Wyser, K., Jones, C.G., Du, P., Girard, E., Willén, U., Cassano, J., Christensen, J.H., Curry, J.A., Dethloff, K., Haugen, J.-E., Jacob, D., Køltzow, M., Laprise, R., Lynch, A., Pfeifer, S., Rinke, A., Serreze, M., Shaw, M.J., Tjernström, M., Zagar, M., 2008. An evaluation of Arctic cloud and radiation processes during the SHEBA year: simulation results from eight Arctic regional climate models. Clim. Dyn. 30, 203–223.
Yeo, H., Park, S.-J., Kim, B.-M., Shiobara, M., Kim, S.-W., Kwon, H., Kim, J.-H., Jeong, J.-H., Park, S.S., Choi, T., 2018. The observed relationship of cloud to surface longwave radiation and air temperature at Ny-Ålesund, Svalbard. Tellus B 70, 1–10. https://doi.org/10.1080/16000889.2018.1450589.
Zhao, P., Zhang, X., Zhou, X., Ikeda, M., Yin, Y., 2004. The sea ice extent anomaly in the North Pacific and its impact on the East Asian summer monsoon rainfall. J. Clim. 17, 3434–3447 doi:10.1175/1520-0442(2004)017<3434:TSIEAI>2.0.CO;2.